

General Disclaimer

One or more of the Following Statements may affect this Document

- This document has been reproduced from the best copy furnished by the organizational source. It is being released in the interest of making available as much information as possible.
- This document may contain data, which exceeds the sheet parameters. It was furnished in this condition by the organizational source and is the best copy available.
- This document may contain tone-on-tone or color graphs, charts and/or pictures, which have been reproduced in black and white.
- This document is paginated as submitted by the original source.
- Portions of this document are not fully legible due to the historical nature of some of the material. However, it is the best reproduction available from the original submission.



July 31, 1974

NASA Scientific and Technical Information Facility
Post Office Box 33
College Park, Maryland 20740

Gentlemen:

Enclosed please find our annual progress report for September, 1973 to August, 1974. I am also sending the renewal proposal on the Micro-electronics Bioinstrumentation System, Research Grant NDR-36-027-053, covering the period from September, 1974 to August, 1975. G

We would appreciate your review of this material, and if any further information is required, please write or call me at area code 216, 368-2934.

Very truly yours,

Dr. Wen H. Ko
Director
Engineering Design Center

WHKo/sw

Enclosures

CC: Dr. H. L. Stone
Dr. H. Sandler
Mr. Ray Sutton
Dr. Stanley Deutsch
Mr. T. B. Fryer



(NASA-CR-139216) MICROELECTRONIC
BIOINSTRUMENTATION SYSTEM Annual Progress
Report, Sep. 1973 - Aug. 1974 (Case
Western Reserve Univ.) 59 p HC \$6.00

N74-29463

Unclas

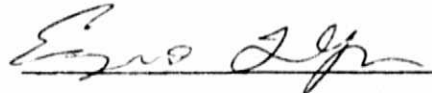
CSCCL 06B G3/05 54722

MICROELECTRONIC BIOINSTRUMENTATION SYSTEMS

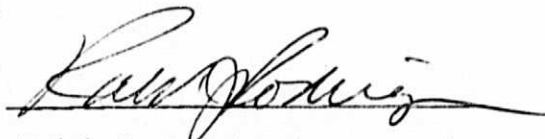
Submitted To
AMES RESEARCH CENTER
NATIONAL AERONAUTICS AND SPACE ADMINISTRATION



Wen H. Ko, Ph.D.
Principal Investigator
Director, Engineering
Design Center



Eugene T. Yon, Ph.D.
Co-Principal Investigator
Associate Director, Microelectronics
Laboratory



Ralph J. Rodriguez
Assistant Director
Research Administration

July 27, 1974

ENGINEERING DESIGN CENTER
Case Institute of Technology
Case Western Reserve University
Cleveland, Ohio 44106

Proposal for Microelectronic
Bioinstrumentation Systems

For the continuation of Research Grant NDR-36-027-053 Microelectronics Bioinstrumentation Systems, for the period September 1, 1974 - August 31, 1975 we propose to perform the following work:

1. R.F Powered Implant Telemetry System

A telemetry system operating by external radiated power, compatible with the previously delivered system will be completed and delivered to Dr. H.L. Stone for evaluation. This unit will operate with a single channel of information.

This work will be expanded to include a second channel of information. This channel will be suitable for use in pressure monitoring. At this point, the telemetry system will be suitable for use with chaired monkeys. Following evaluation of this unit, a powering system suitable for free-ranging animals (limited to an over-all volume of one cubic meter) will be completed and evaluated with the existing telemetry system.

2. Ingestible Telemetry System

Work in this area will continue with the examination of the possibility of radio frequency powering. Exploratory work involving the possibility of using pH electrodes with the present unit will begin. During this phase of the work, the packaging of the unit will be refined. Some preliminary work has been started in the investigation of the possibilities of fabricating this unit using monolithic circuit techniques.

3. Implant Stimulator Unit

Research into the development of an implantable stimulator unit will begin during the contract period. The alternate goal of this work will be the fabrication of reliable stimulator implants suitable for external control by radio

link. The planned work for this period will involve the evaluation of several concepts that can be used for the supply of variable current duration and frequency stimulation pulses, sequentially to a series of electrodes. Following this evaluation, a selected prototype will be constructed for preliminary performance determination. It is planned that this work will be expanded in the future to include construction of implantable units and evaluation in animals

ANNUAL REPORT FOR RESEARCH GRANT NDR-36-027-053
Microelectronics Bioinstrumentation System
April, 1973 to June 1974

Submitted to National Aeronautics Space Administration

Dr. Wen H. Ko
CASE WESTERN RESERVE UNIVERSITY
Case Institute of Technology
Cleveland, Ohio 44106
July 27, 1974

This report covers the progress made from April 1973 to June 1974, the second year of Research Grant ~~NOR~~^{NSF} -36-027-053, entitled Microelectronics Bioinstrumentation System. As proposed, the research for this period covers:

1. R.F. powered implant telemetry system
2. An ingestible temperature telemeter
3. Development by pO_2 and pH sensors.

The progress report is divided according to those three projects.

i. RF-POWERED LONG TERM IMPLANT TELEMETRY SYSTEM FOR ANIMAL STUDY

1A General System and Implant Unit

1) Background

An RF powering scheme was selected to supply the power for the Implantable telemetry System. In order to use only one RF tank circuit in the implant unit the same frequency is used to power the implant and to send back the data. The timing diagram is as follows : (Fig. 1)

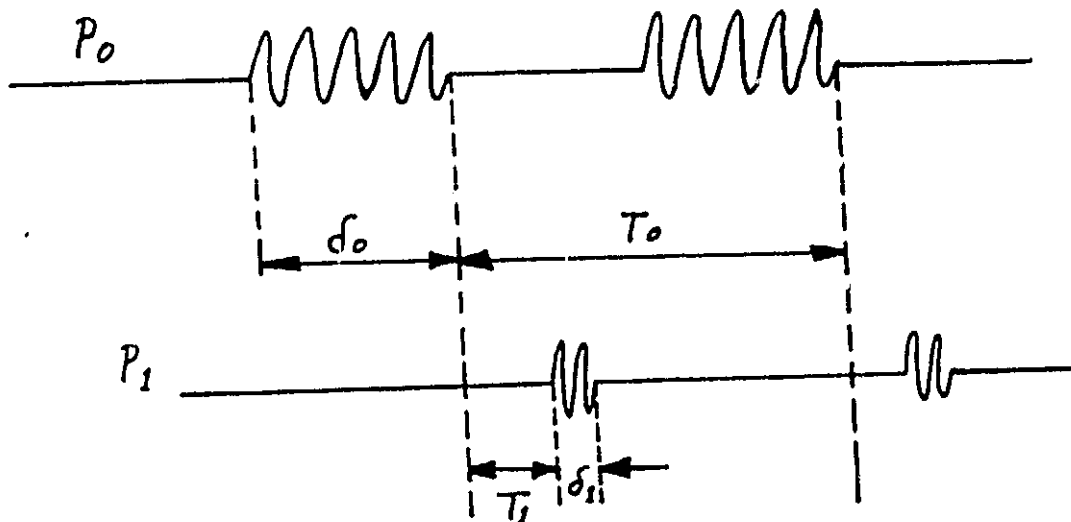


Fig. 1 Timing diagram for RF-powering

The information is coded in the position T_1 of the RF burst transmitted by the implant. Since the implant senses the trailing edge of the power pulse P_0 and uses it as a synchronization for modulation, the system is thus insensitive to the duration of the power pulse δ_0 as well as to the period T_0 .

The condition which must be satisfied for T_0 is: $T_0 > T_1 \text{max} + \delta_1$

On the other hand, it is not desirable to use up all the energy supplied into the implant during the application of P_0 , this means that T_0 shouldn't be much larger than $T_1 \text{max} + \delta_1$. The length of the power pulse δ_0 is not critical, and its variations will not introduce any error into the data transmission. There is only minimum requirement for δ_0 in order to be sure that the implant is fully charged after every δ_0 pulse, $\delta_0 > \delta_0 \text{ min}$.

2) System Block Diagram:

The System operation can be seen from the following block diagram:

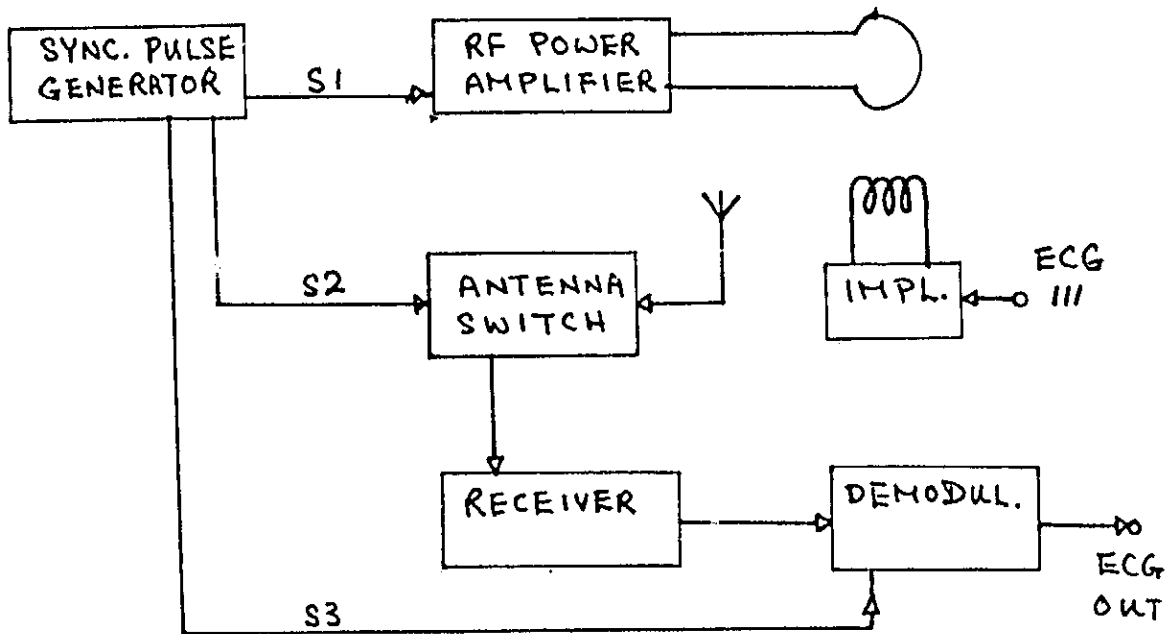


Fig. 2 RF-powered system block diagram

The RF signal is generated in the "synch pulse generator" and is further amplified by RF power amplifier to the desired power level. At the same time, two more pulses are generated. The first, S_2 , to block the input of the receiver

and protect it from overloading, and the second, S_3 , which is used to reset the demodulator. The timing diagram for the pulses S_1 , S_2 and S_3 is in Fig.3.

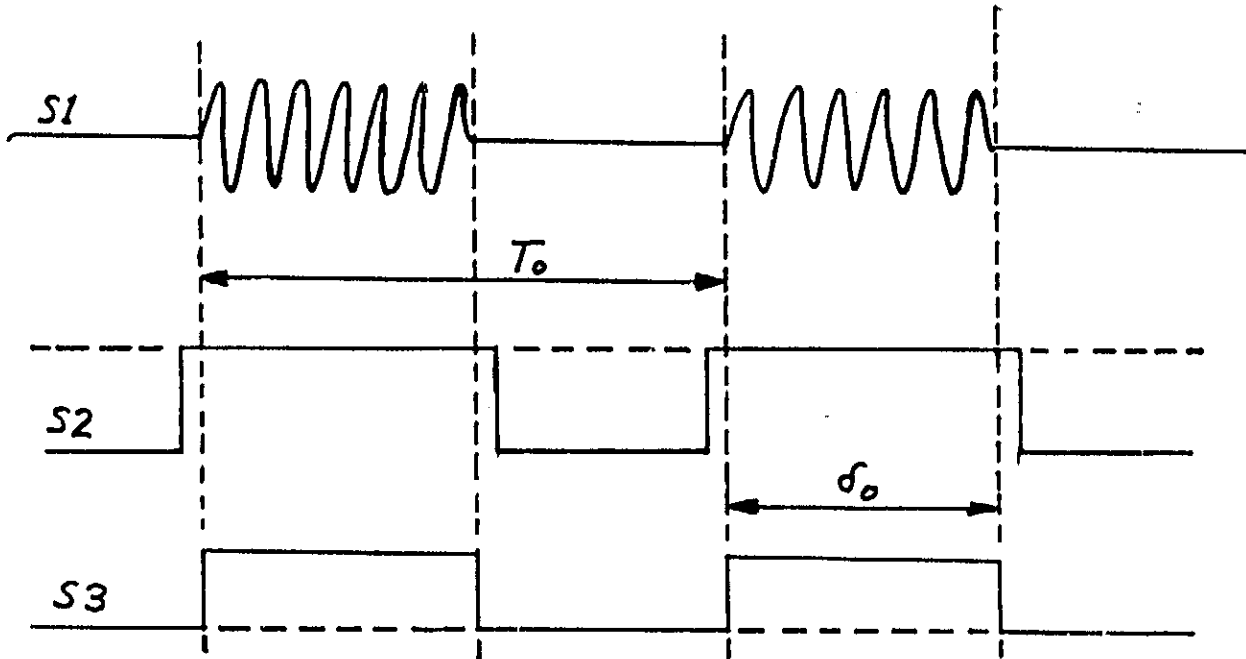


Fig.3 Synchronizing pulses timing diagram

The pulse S_2 for controlling the antenna of the receiver is slightly overlapping the pulse δ_0 in order to compensate for possible propagation delays in the RF power amplifier.

3) Antenna Switch:

The antenna switch circuit diagram is seen in Fig. 4:

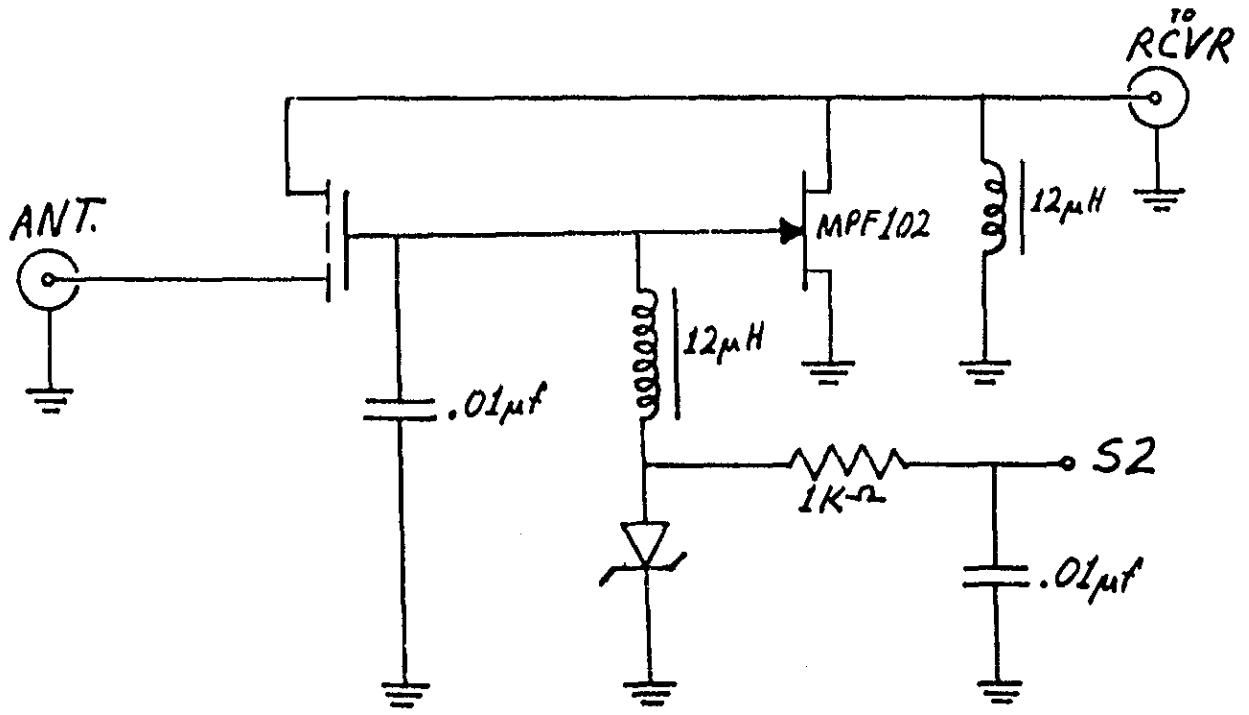


Fig. 4 Circuit for antenna switch

The function of the circuit should be from the above circuit diagram. Signal rejection was found to be more than 50 dB in the off state, which is quite satisfactory for our purposes.

4) Demodulation:

The circuit diagram of the demodulator is shown in Fig. 5:

ramp appears at TP1. When the receiver output supplies the pulse from the implant, the ramp at TP1 is sampled and the voltage is stored on the capacitor with the second operational amplifier. In this manner the position of the pulse from the implant is converted into the voltage which appears after proper level shifting at the demodulator output. There are two potentiometers in the circuit. R1 serves as a base line adjustment by changing the amount of level shifting and the R2 adjusts the demodulating range (rate of charging Cx). Adjustment of R2 should be done in such a way so that the the ramp at TP1 will not be saturated when $T_1 = T_1 \text{max}$. The rest of the circuit serves as signal processing for the pulse received from the implant. There is an input polarity switch and floating threshold limiter.

5) Implant Circuit Description:

The implant transmitter block diagram is shown below.

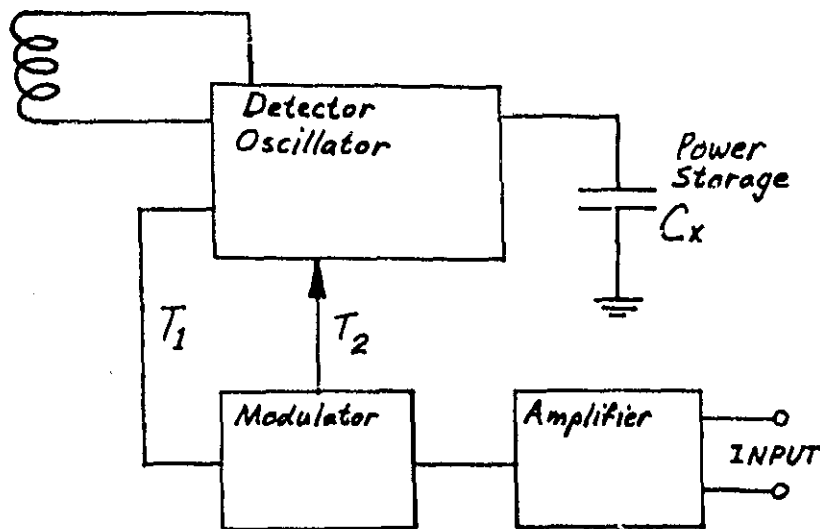


Fig. 6 Implant transmitter block diagram

The function of the implant is as follows: after the detector-oscillator detects the trailing edge of the power pulse, P_o , the trigger pulse, T_1 , is generated and sent into the modulator. The modulator is reset and the trigger pulse for the oscillator is generated corresponding to the amplifier output voltage. The amplifier circuit diagram is in Fig. 7.

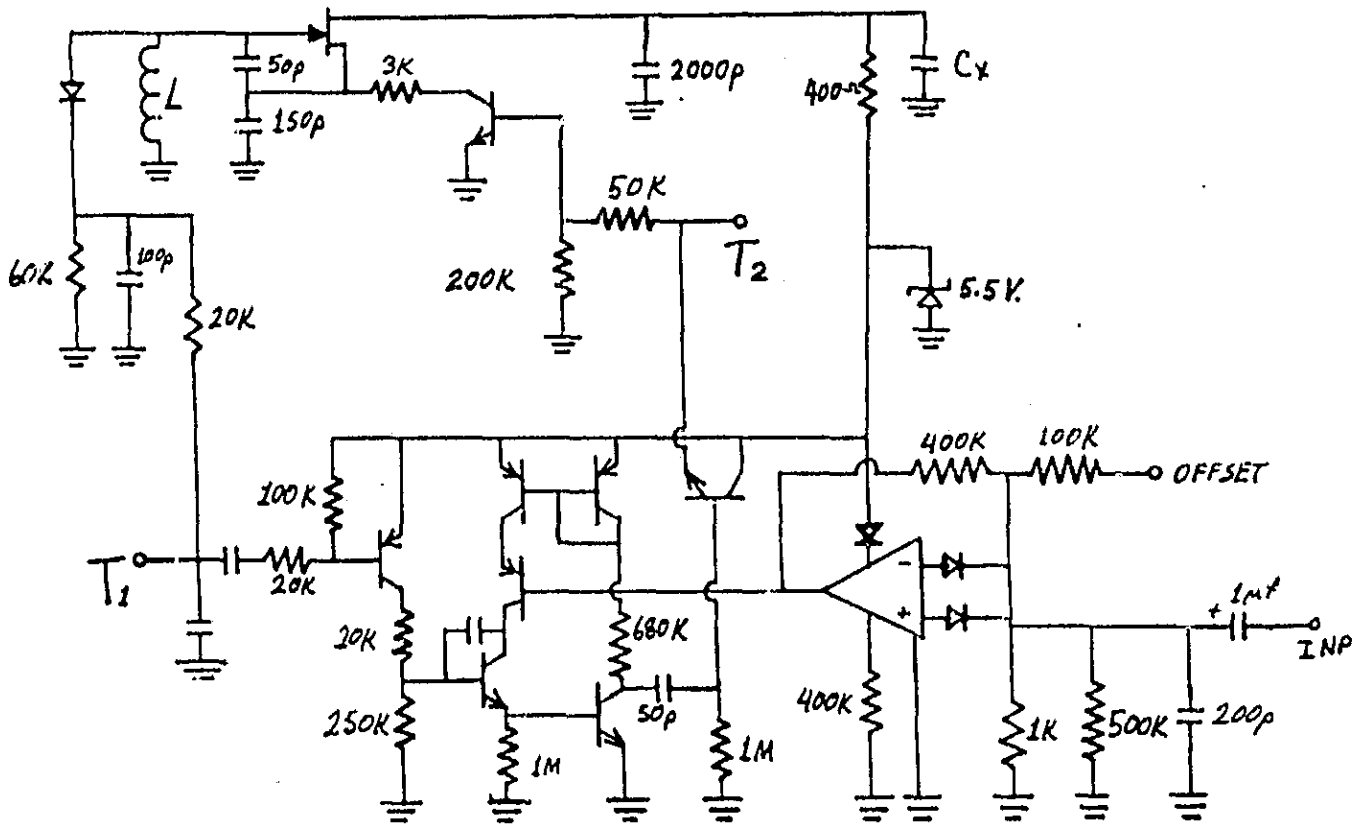


Fig. 7 Implant circuit diagram

The circuit was built in three flat packs with two external components; storage capacitor C_x and offset resistor to adjust the zero for ECG amplifier. As of this date, the implant unit has been finished and is awaiting final test.

1B External Power System

This section summarizes the status of support hardware and electronics required to RF power an implanted biotelemetry transmitter. Design goal for the total DC power requirement to the implant package is 3.6 milliwatts (6v at 600 microamperes). The animal under observation is enclosed by a 1 meter cubical resonator which is driven by 30 MHz pulsed RF. The drive is pulsed at 200 Hz, with 40% duty cycle, to provide periodic 3 msec data output windows.

The cubical resonator has been constructed from 1/32 inch aluminum panels over a rigid frame of 1 1/2 inch aluminum angle stock. The enclosure can be readily disassembled for modification or shipment. Figure 8 shows the resonator in its present form, including the drive antenna designed to produce a uniaxial magnetic field at 30 MHz. The antenna consists of four 0.5 inch diameter copper rods, each series tuned by a 50 pf variable capacitor. This structure, tapped 2 inches from one wall of the enclosure, forms two one-turn coils driven in phase. Input power from a 50 ohm coaxial feed was coupled into the resonator via a 1:1 unbalanced - to - balanced resonant transformer.

Initial tuning of the resonator was performed with the aid of the field strength probe shown in Figure 9. The ten turn pickup coil which has the same capture aperture as that in the implant (0.75 sq. in.), was placed near the center of the resonator and oriented for maximum coupling. Detector output reached 10 volts DC at an RF input power of 2w. to the resonator. The drive point VSWR, as measured by a coaxial reflectometer, was close to 1:1 at resonance. Plots of detector output voltage VS coil position along several transverse planes within the enclosure are shown as Figure 10. It should be

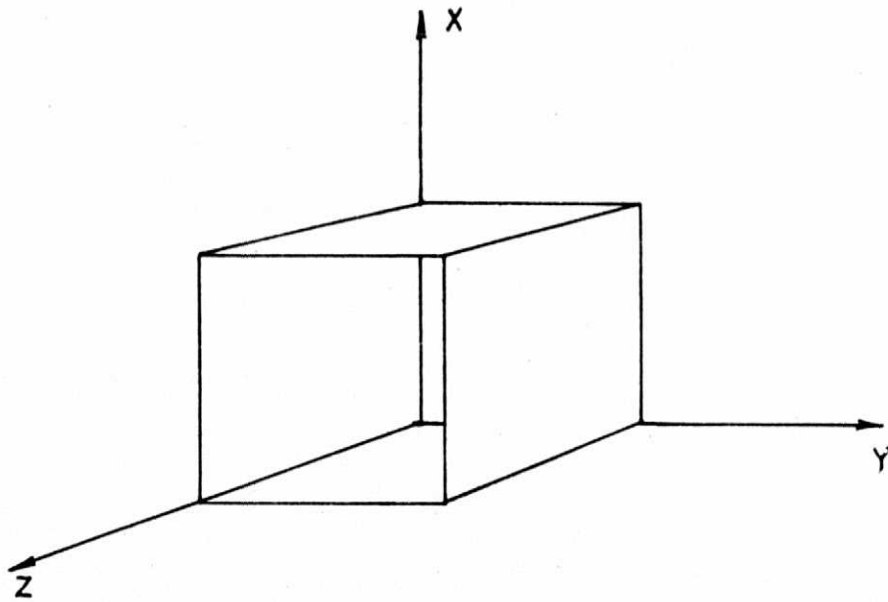
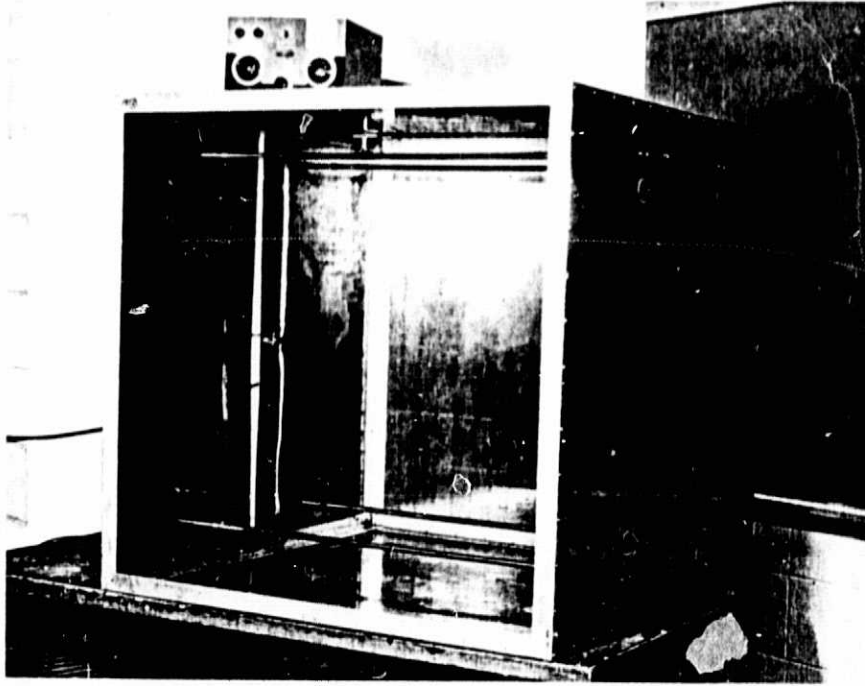


Fig 8a

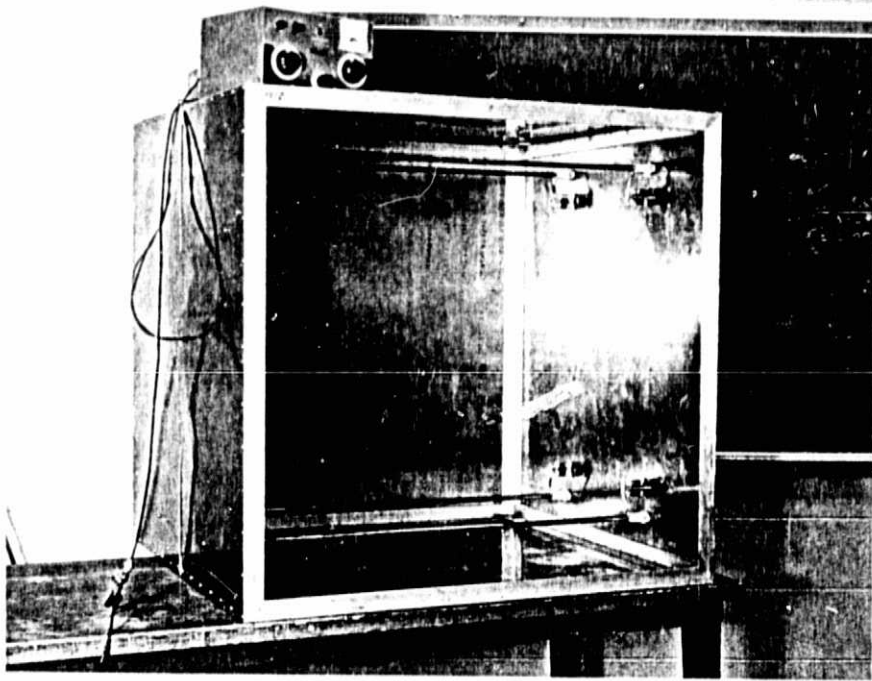


Fig. 8b

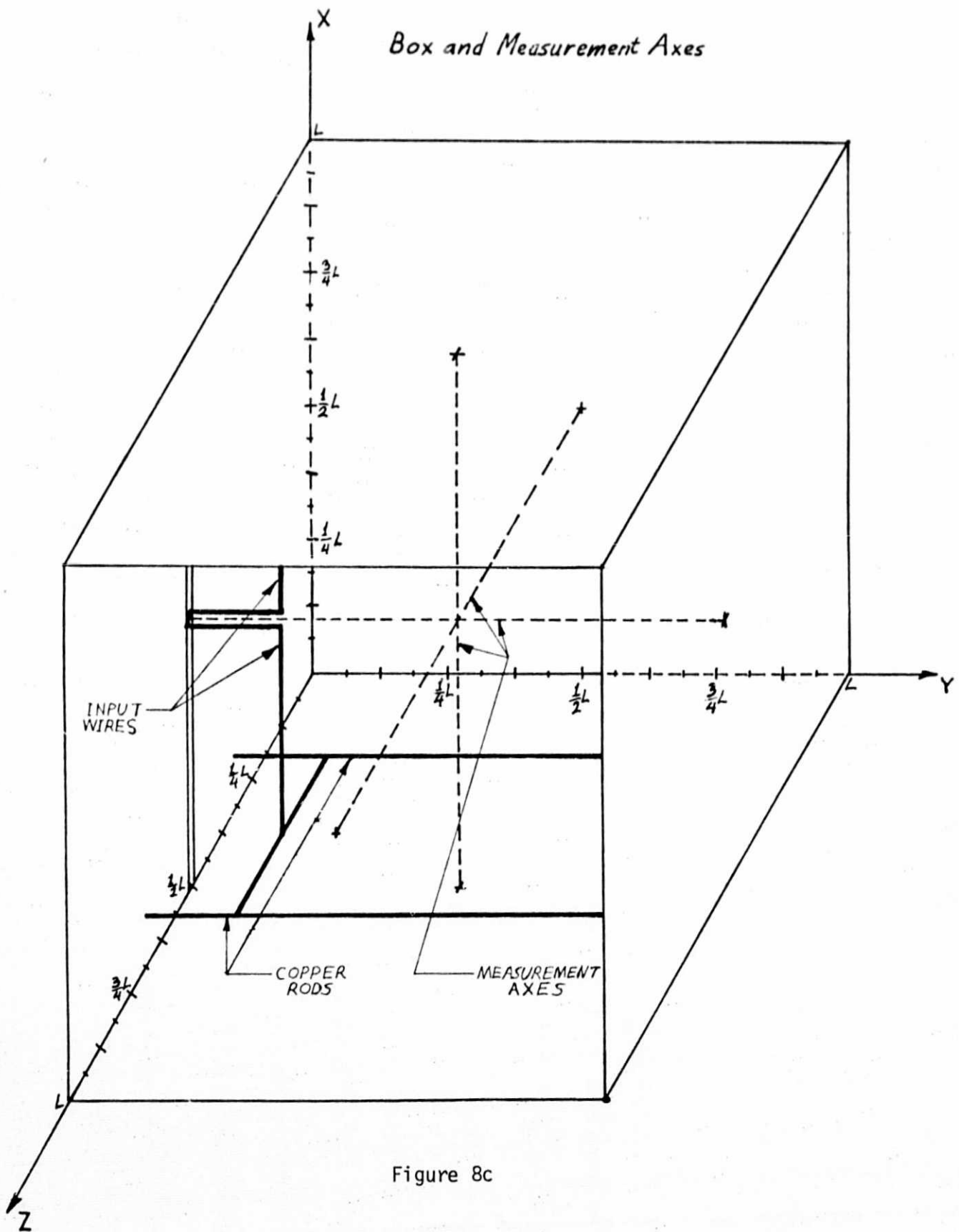


Figure 8c

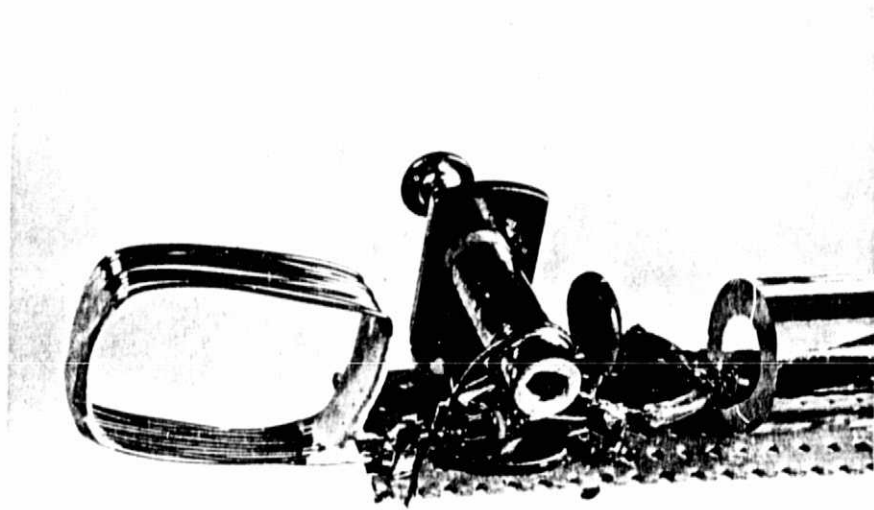
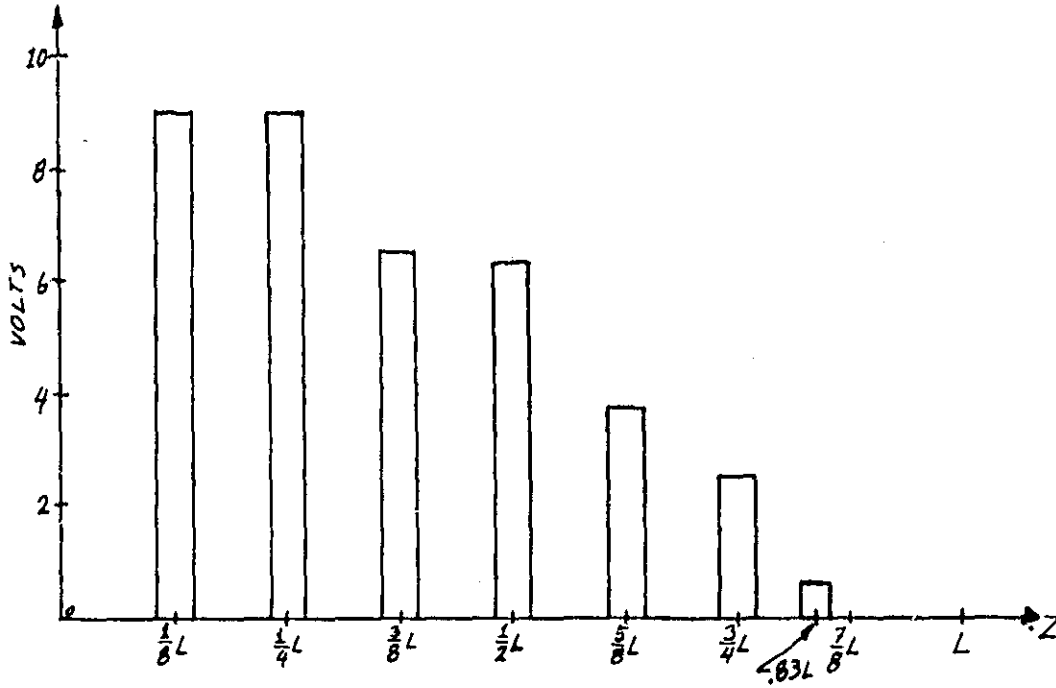


Fig. 9

PICKUP VOLTAGE FOR
Z-DIRECTED MAGNETIC FIELD (~30 MHz, 10w)
WHEN $X=Y=1/2L$



FOR THIS AND FOLLOWING GRAPHS.
 $L = 1$ METER, THE TOTAL LENGTH OF ANY EDGE OF THE BOX.

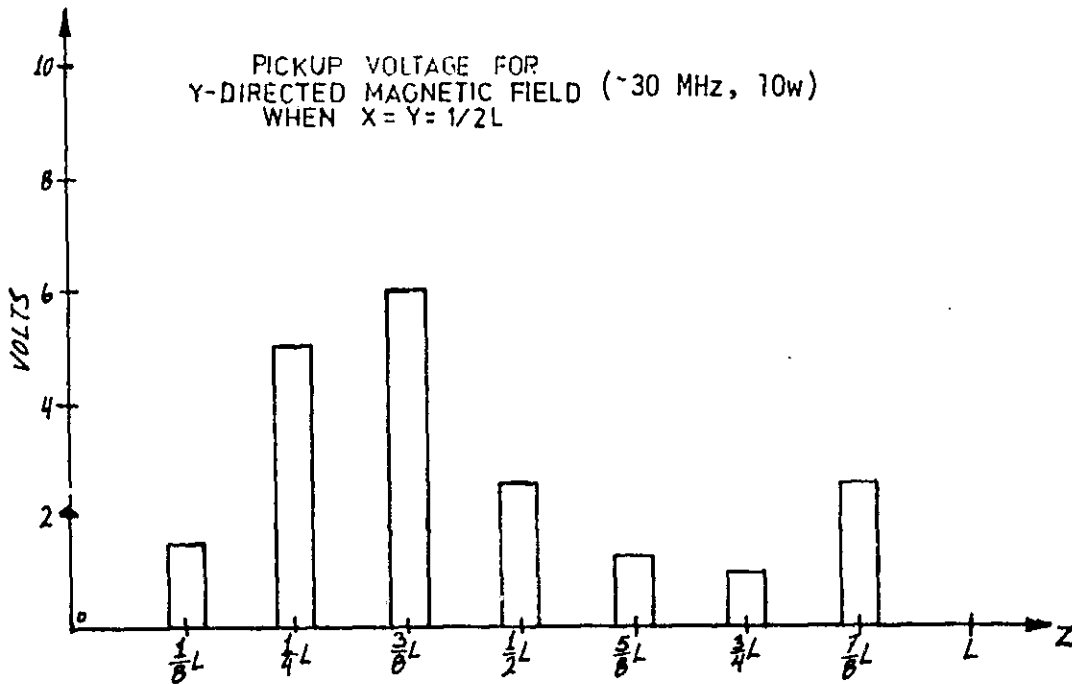


Fig 10a

PICKUP VOLTAGE FOR
X-DIRECTED MAGNETIC FIELD (~30 MHz, 10w)
WHEN $X=Y=1/2L$

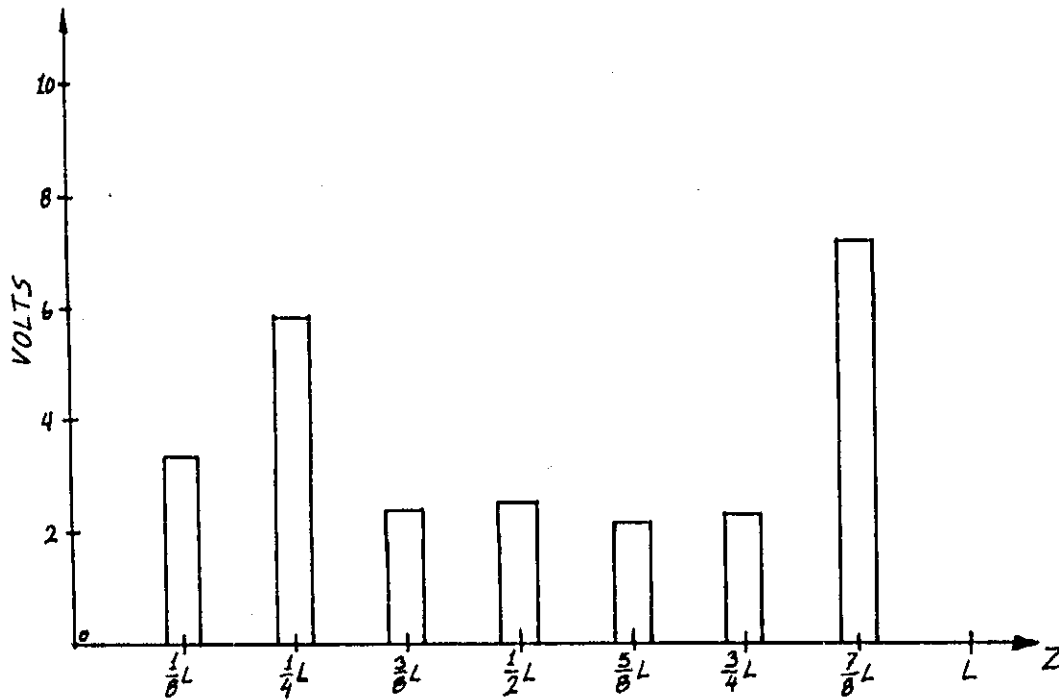
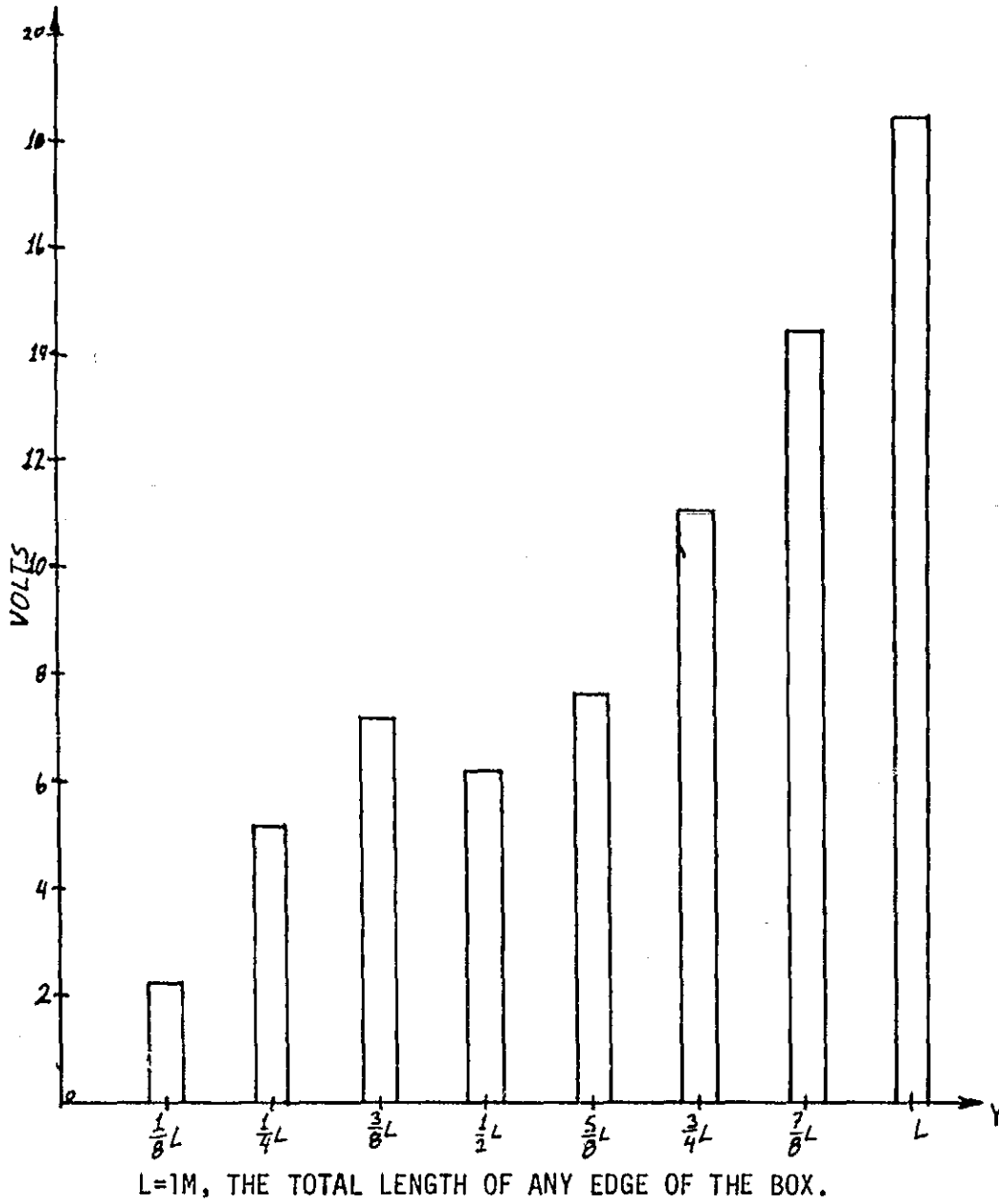


fig 10b

Pickup Voltage For
Z-Directed Magnetic Field (~30 MHz, 10w)
When $X=Z=\frac{1}{2}L$

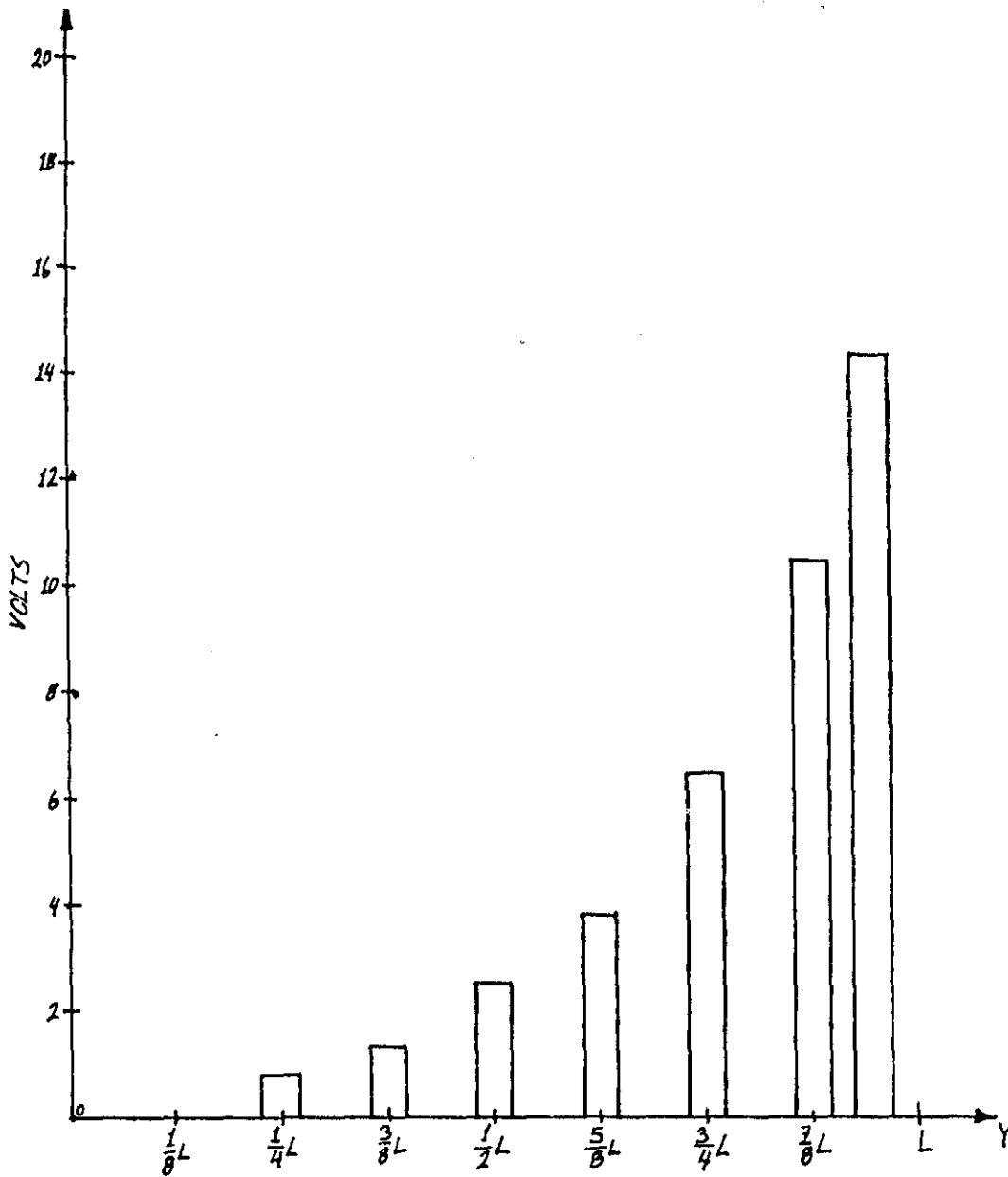


$L=1M$, THE TOTAL LENGTH OF ANY EDGE OF THE BOX.

Fig 10c

Pickup Voltage For
Y-Directed Magnetic Field

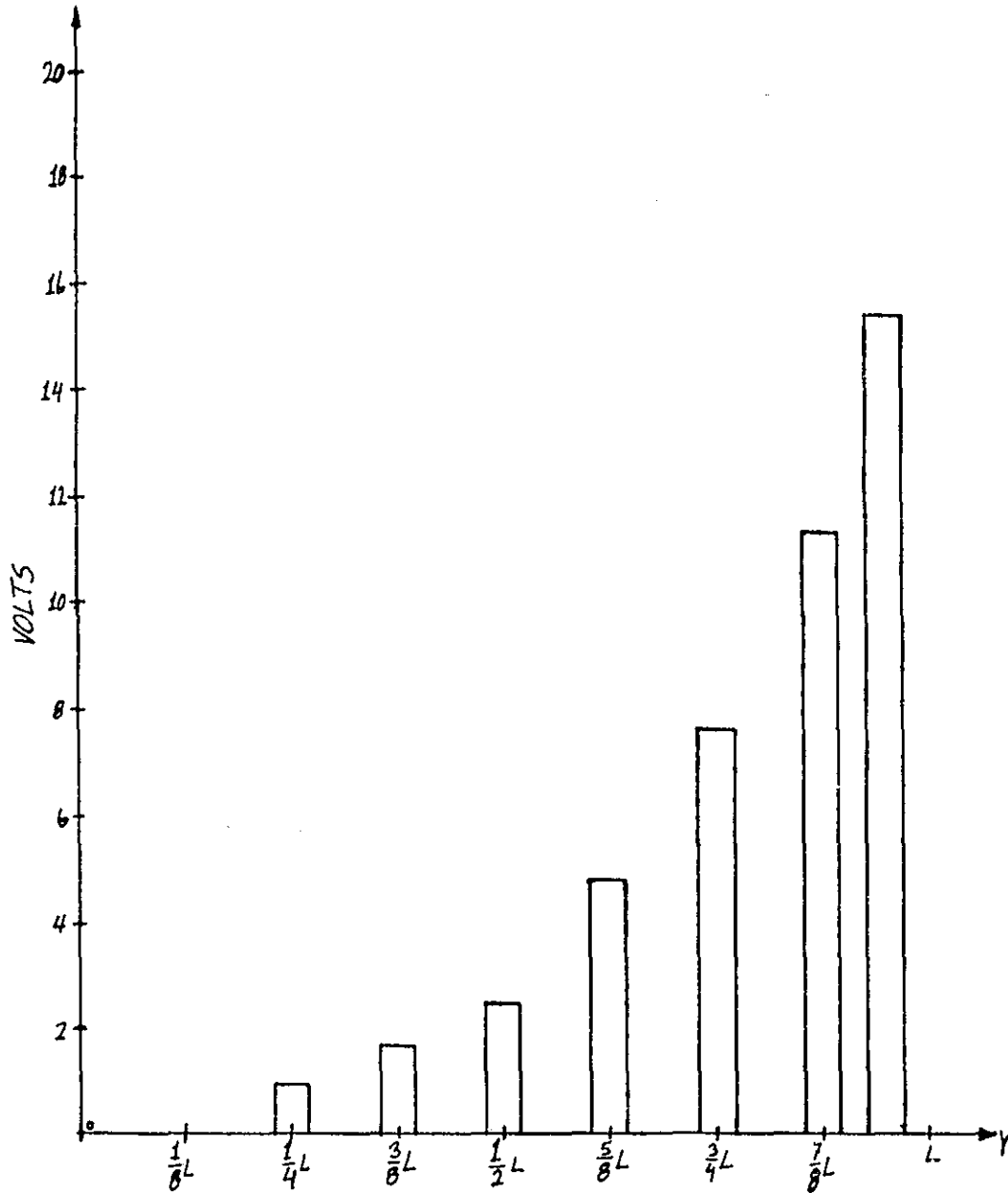
When $X = \frac{1}{2}L$ And $Z = \frac{1}{2}L + 2\frac{1}{4}''$



$L=1M$, THE TOTAL LENGTH OF ANY EDGE OF THE BOX.

Fig 10d

Pickup Voltage For
X-Directed Magnetic Field
When $X=Z=\frac{1}{2}L$

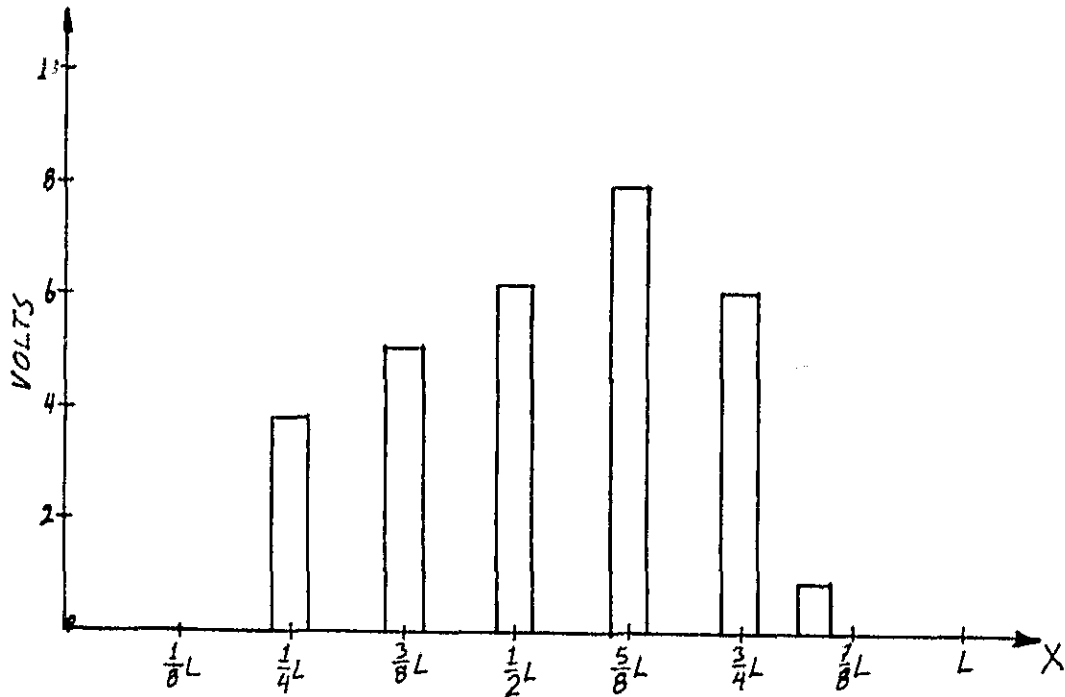


$L=1M$, THE TOTAL LENGTH OF ANY EDGE OF THE BOX.

Fig 10e

Pickup Voltage For
Z-Directed Magnetic Field
When $Y=Z=\frac{1}{2}L$

-18-



$L=1M$, THE TOTAL LENGTH OF ANY EDGE OF THE BOX.

Pickup Voltage For
Y-Directed Magnetic Field
When $Y=\frac{1}{2}L+2\frac{1}{4}$ and $Z=\frac{1}{2}L$

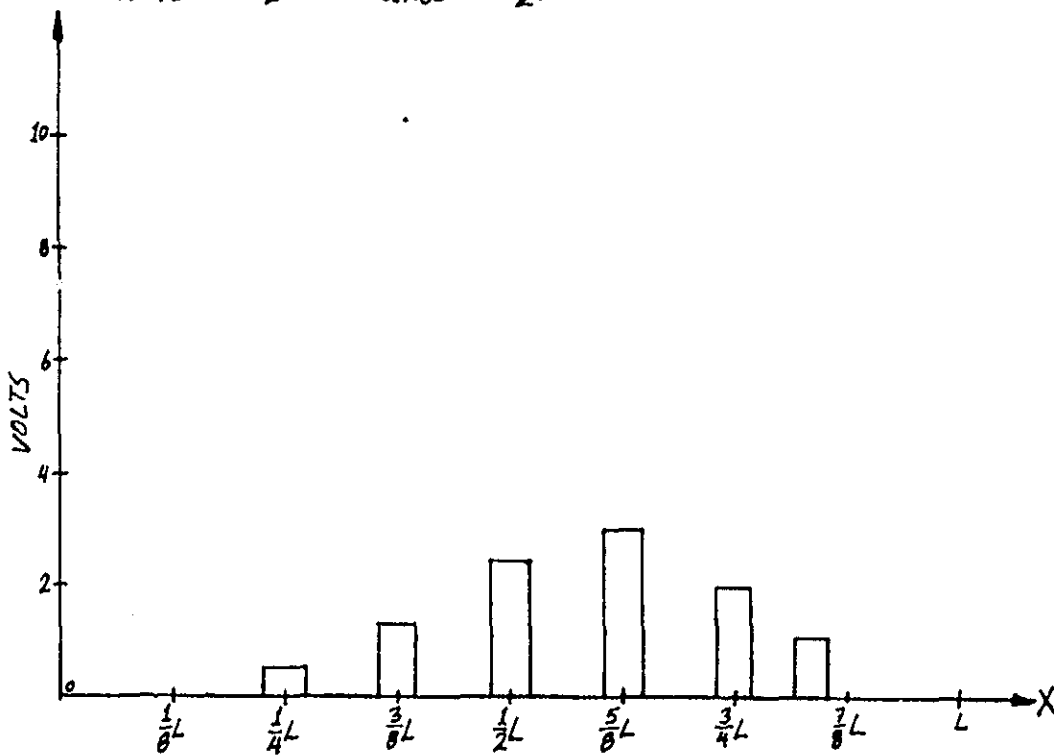
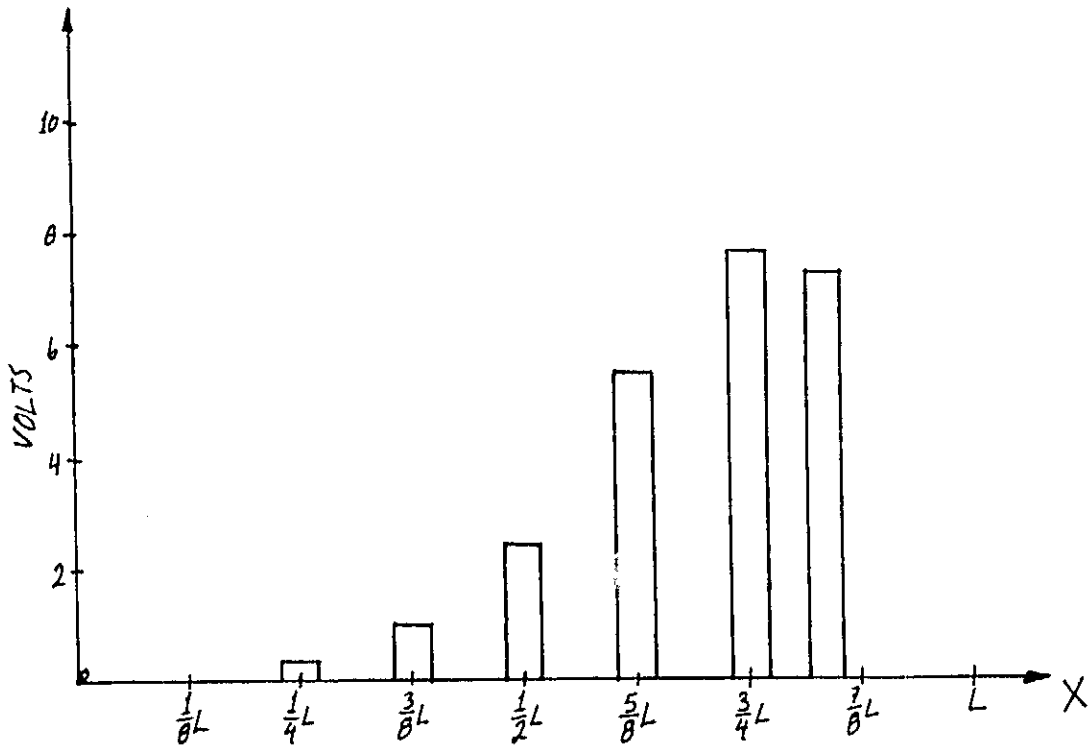


Fig 10f

Pickup Voltage For
X-Directed Magnetic Field ($\sim 30\text{MHz}, 10\text{w}$)
When $Y=Z=\frac{1}{2}L$



$L=1\text{M}$, THE TOTAL LENGTH OF ANY EDGE OF THE BOX

Fig. 10g

noted that the removal of the front cover of the enclosure resulted in a 60 dB reduction of detector output. This drop in signal is attributed to reduction of Q as well as detuning of the structure. Adequate RF continuity of the enclosure has been provided to avoid this effect during normal operation of the drive system.

By reorientation of the pickup loop axis, it was possible to measure each orthogonal component of the driven magnetic field. While the previously reported theoretical development indicated a uniaxial field (here indicated as the z-component), measurements show strong field components along the x and y axis as well. Parasitic field contributions, probably arising in practice as a result of unavoidable electrical asymmetries in the resonator, are shown in Figure 10. Readjustment of the four tuning capacitors had little effect on the relative magnitude of the x-or y- directed fields as compared with the z component. In its present configuration, the wall of the resonator adjacent to the feed contains a vertical slot (1cm x 100cm) to permit probe access. Since the slot lies along the x-axis, it offers no hindrance to the surface currents required to maintain the expected z-axis magnetic field. The final design for the enclosure includes a solid panel to replace the slotted one. This may lead to modification of parasitic mode amplitude distribution. Elimination of the slot will permit z - directed current to flow in the enclosure wall, and an increase of magnetic field strength along the x axis. As described later in this section, the presence of the unexpected parasitic modes can be used to advantage in subsequent project development. If replacement of the slotted wall described earlier should result in sizeable reduction of x- and y- axis magnetic field components, the enclosure can be modified to include one or more appropriate slots to re-establish these modes.

Since the radiated power from the implant is of low level, it is essential that residual RF power remaining in the enclosure after the drive pulse terminates be highly damped. The RF source employed during the experiments reported here could be pulsed at the required rate and duty cycle, but produced output pulses with rise and fall times of 200 μ sec. To better evaluate performance of the resonator itself, quality factor Q was calculated from a measurement of system bandwidth. The measured Q of the field probe (and that of the implant as well), is ~ 7 . Since this is much lower than that of the resonator, the latter has dominance in determining damping time. Measured bandwidth at -3dB point is ~ 100 KHz, indicating a loaded Q of 300. Conservatively estimating power input to the resonator of 10 Watts and implant radiated power of 1 picowatt, one finds that the time required for drive power to decay to .01 pw (i.e., for +20 dB S/N) is approximately 40 time constants, or less than 2 msec. This shows that even the empty resonator is sufficiently lossy to avoid signal to noise problems resulting from ringing. Placing a dielectric cage and laboratory animal into the resonator will introduce additional loss, reducing Q somewhat. It should be pointed out that this additional loss will be small, since the magnetic drive produces low amplitude electric field strengths, and correspondingly low dielectric losses.

It should be noted that if both the driven field and the implant antenna response patterns were one dimensional, the telemetry system would function only in those intervals during which the antenna pairs were aligned sufficiently for minimum coupling. At other times, angular drift of the animal's relative to the enclosure would prevent efficient coupling of RF drive to the implant. If the drive field was truly uniaxial, the requirement that the system perform for any arbitrary angular orientation of the animal could be met only through addition of two more drive antennas and associated electronics. The observed three component nature of the present drive field is therefore not unwelcome.

This will be driven via inductive coupling from a coil behind the chair. A solid state driver capable of 10 watts of RF output is presently undergoing testing. Figure 11 shows the circuit used as a 60 MHz amplifier.

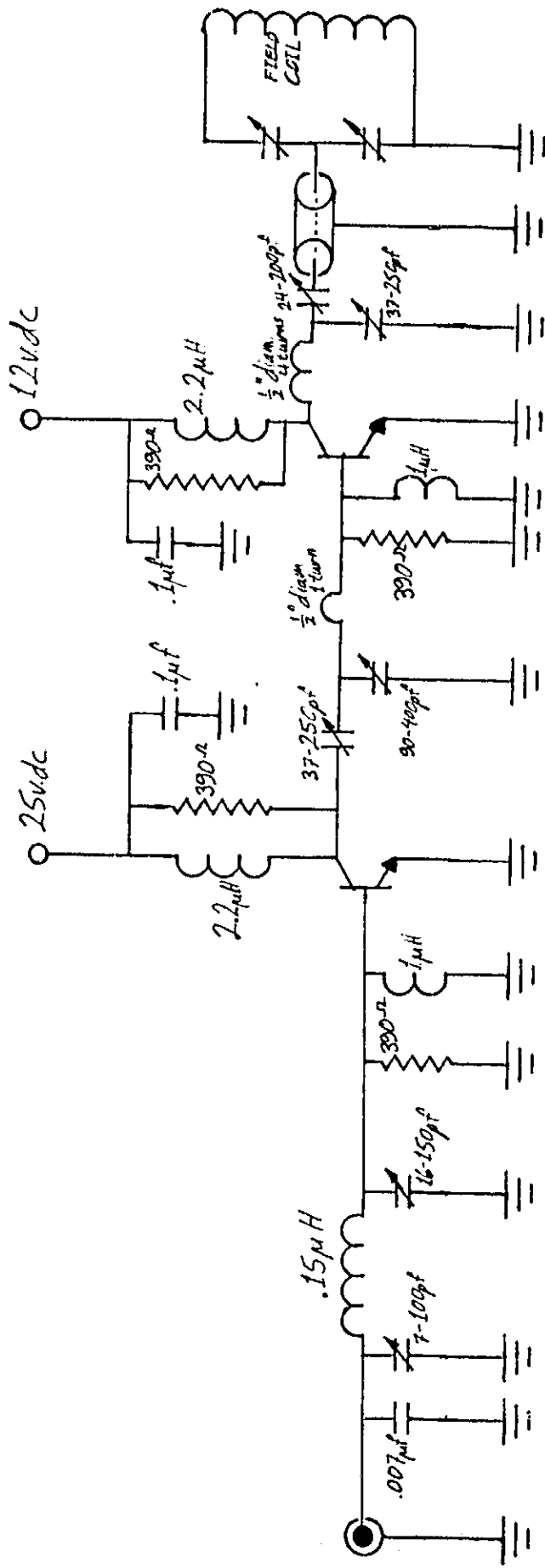


Fig 11

II. INGESTIBLE TEMPERATURE TELEMETRY SYSTEM

This part of the report summarizes the progress made on the development of an Ingestible Temperature telemetry system following the last semi-annual report of December, 1973. This report includes the Pulse Frequency Modulator of the transmitter and the digital processing unit of the receiving unit.

1. Pulse Frequency Modulator

The original M-4 circuit had the draw-back of high current drain at low temperature range (see semi-annual NASA Research Report on Microelectronics Bioinstrumentation System of December, 1973. Grant number NDR-36-027-053). This impedes the possibility of low temperature storage to cut down power consumption and to extend battery life time.

The development of the M-6 circuit pushed the low temperature high current drain state below the normal refrigerator temperature. The M-6 circuit had the drawback that the pulse width is increased due to the addition of the diode D₁. (Fig. T1) This increases the duty cycle and the power consumption.

One approach to this problem is to cut off the base current of Q₁ abruptly. This had led to the development of the M-7 circuit. (Fig. T2)

The M-7 circuit is basically the same as the M-6 circuit with the addition of Q₃, R₄ and R₅. During the "ON" cycle of Q₂, V_{out} keeps Q₃ "ON" and i_{c3} acts as a current sink to i₁. This current sink scheme is able to shorten the pulse width of the circuit and by proper selection of R₄ and R₅ the pulse width can be controlled to within a specified range. (Fig. T3)

During the initial charging cycle of C₁, the base to collector junction diode of Q₃ becomes forward biased. Thus a leakage current i_L will tend to charge up C₁ in addition to i_T. This leakage current will stop as soon as the Q₁ side of C₁ charges up to the negative value of one diode drop (collector to base junction diode of Q₃). Theoretical analysis on the effect of leakage current shows that the

pulse period vs. temperature calibration the M-7 circuit has an upshift with respect to the one without the current sink circuit (Fig. T4). Test on the M-7 reveals no drawback in circuit performance.

The packaged M-7 transmitter has typical performance characteristics as given in the table T1.

2. Receiving System

The old design of the receiving system was reported in the 1972-73 NASA Progress Report on Microelectronics Bioinstrumentation Systems, April 1973.

Since then several improvements have been made. These are summarized as follows:

DIGITAL PROCESSING UNIT (Fig T5)

The modified digital processing unit was built and is under testing. The unit consists of five boards:

- A. Control logic board (Fig. T6)
- B. Pulse Period Discriminator board (Fig T7)
- C. Digital counter and logic board (Fig T8)
- D. D/A converter board
- E. Power Supply board

Brief description of these boards are given below:

A. Control Logic Boards:

This board performs the following functions

- A. Pulse amplitude discrimination (Fig. T9)

This discriminator is the first series discrimination scheme in the processing unit. The capacitor C_1 charges up to the incoming pulse amplitude through the buffer OA1. OA3 is intended to compensate for the voltage drop of R_1 and base to emitter junction diode of Q_1 . The intended threshold for discriminating an incoming signal is adjusted by R_8 and COMPI acts as the comparator.

b. Pulse width discrimination (Fig T6)

This discriminator consists of monostable multivibrators MM1 and MM2 whose pulse width are preset at t_1 and t_2 respectively. This will set up a time window for acceptance of a pulse with pulse width τ satisfying $t_1 < \tau < t_1 + t_2$.

c. Error Counter (Fig T6)

The error counter counts the number of pulses coming in once an error signal beyond the acceptable pulse period range is detected.

During the counting period there will be no pulse output and the digital display will keep the last acceptable value on display. The error counter will be filled by 7 counts (1-1-1) and the pulse period discriminator will be cleared to restart its function. Thus the error counter is able to discriminate a sudden burst of error signals (less than 7 counts).

d. Logic Circuitry (Fig. T6)

This acts as the interfacing unit between the different discrimination scheme to perform the desired functions.

B. Pulse Period Discriminator board (Fig T7)

This discriminator will store the last incoming pulse period and compare it with the present signal. A presettable range of period width will allow the discrimination between expected pulse period variation and noise signal. This unit combines with the control logic unit will perform the desired pulse period discrimination.

C. Digital Counter and Logic (Fig T8)

This unit consists of a timing circuitry which will gate the display from 0.5~ 15 sec. interval. The counter is a presettable unit such that a reference number can be dialed in (such as the 37°C normal body temperature). This enables the display to show the variation to the preset reference. Thus the

sensitivity of the counter can be increased with the same number of digits and variation in body temperature can be easily recognized.

D. D/A Converter

This will be commercially available module and will convert the digital output as on the digital display to analog signal. This allows the analog display of the temperature information as well as storage on chart recorder.

Future goal

For long term implantation purpose it is desirable to avoid the use of battery power. Therefore it will be our future goal to investigate and evaluate the possibility of using external R. F. powering scheme for the temperature transmitter. The different problems that has to be studied theoretically and experimentally will include:

- A. Power requirement and power scheme (continuous vs. intermittent).
- B. Coil size
- C. Packaging

Whether it is worthwhile to use the R. F. powering scheme has to be studied through experimentation

2. When the desired pH and pO_2 electrodes are available we will investigate the feasibility of interfacing them with the temperature sensor for a more versatile biomedical sensor.

TABLE T-1 M-7 Transmitter Performance Characteristics

Characteristics	Value	Remark
Size, diameter	0.22"	{ Includes battery
length	0.28"	
Weight	1 3/4 gm	"
Power Supply	1.35 V	212 Mercury Cell
Power drainage	3-6 μ A	{ 25°C ~ 50°C
	4-8 μ A	
Radio frequency, f	130 MHz	25°C ~ 50°C
Pulse Width, τ	10 msec	25°C ~ 50°C
Pulse period, T	3600 msec	Measured at 37°C
Sensitivity, $\Delta Z/\Delta f$	95 m sec/°C	Measured at 37°C
Straight line linearisation at 37°C	<0.05°C	maximum in the +5°C extremity
	\pm 0.5 Mlt	in a day
Stability Δf ΔZ	\pm 10 msec	Equivalent to \pm 0.05°C at 37°C

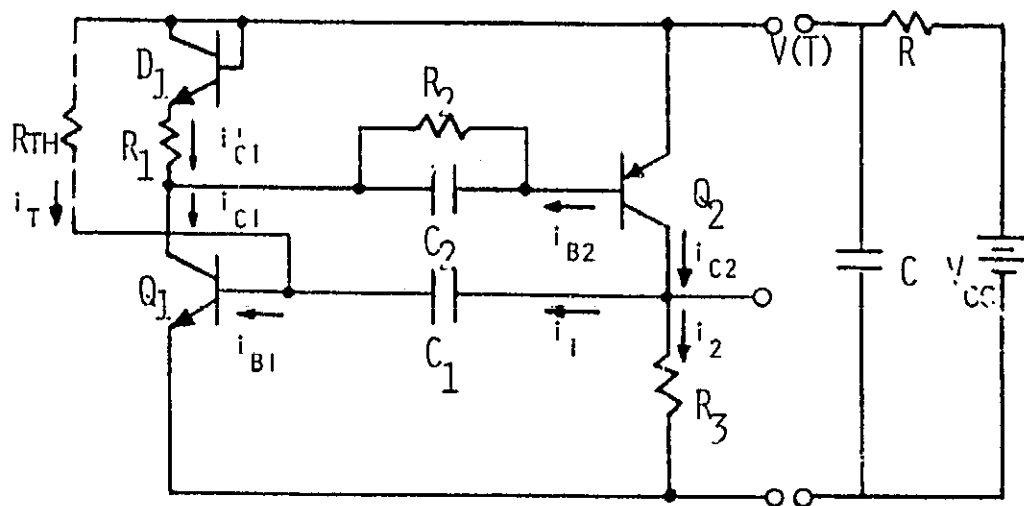


FIG. T 1 M-G PULSE FREQUENCY MODULATOR WITH EXTERNAL RC

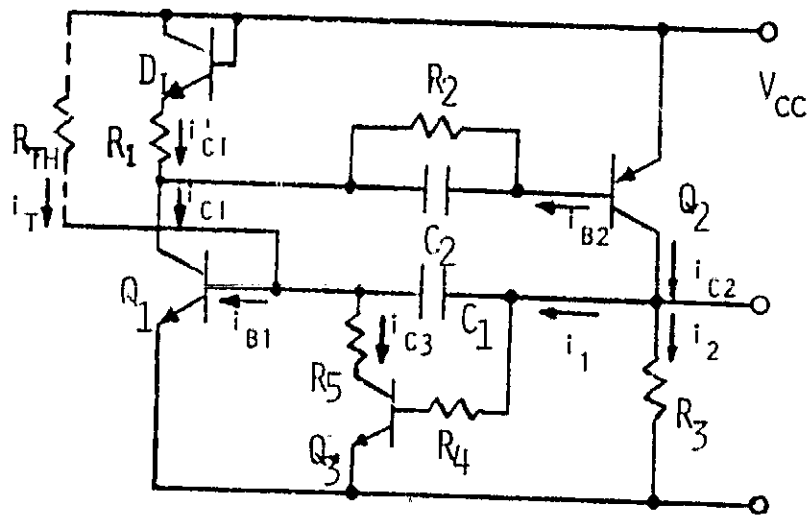


FIG. T 2 M-7 PULSE FREQUENCY MODULATOR

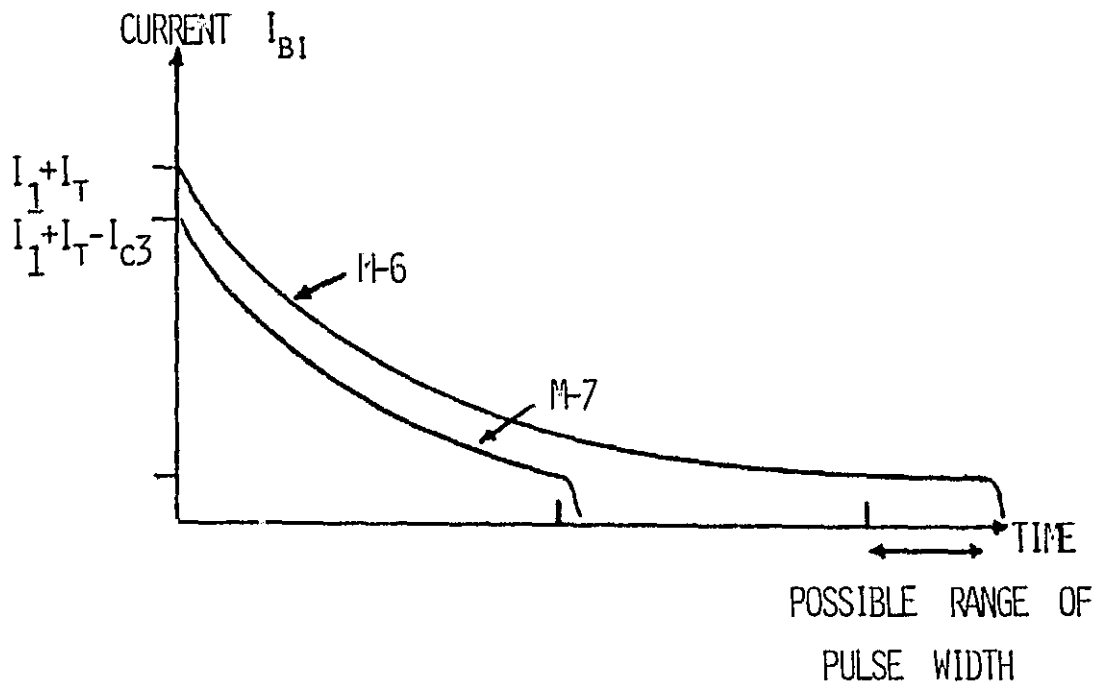


FIG. T 3 BASE CURRENT, I_{B1} , OF TRANSISTOR Q_1 VS. TIME
SHOWING PULSE WIDTH VARIATION OF M-6 & M-7

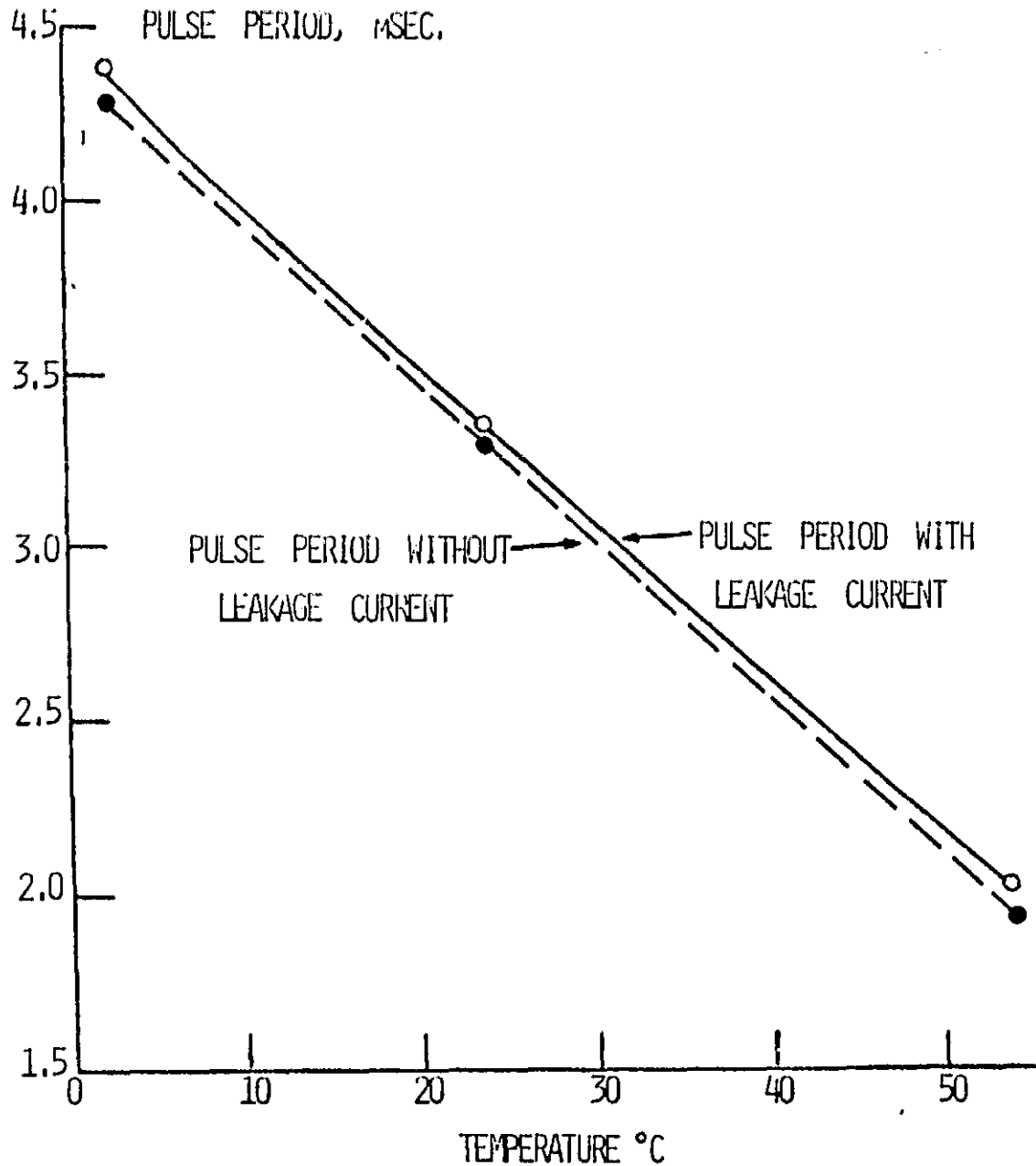


FIG. T 4 THEORETICAL CURVE OF PULSE PERIOD VS. TEMPERATURE

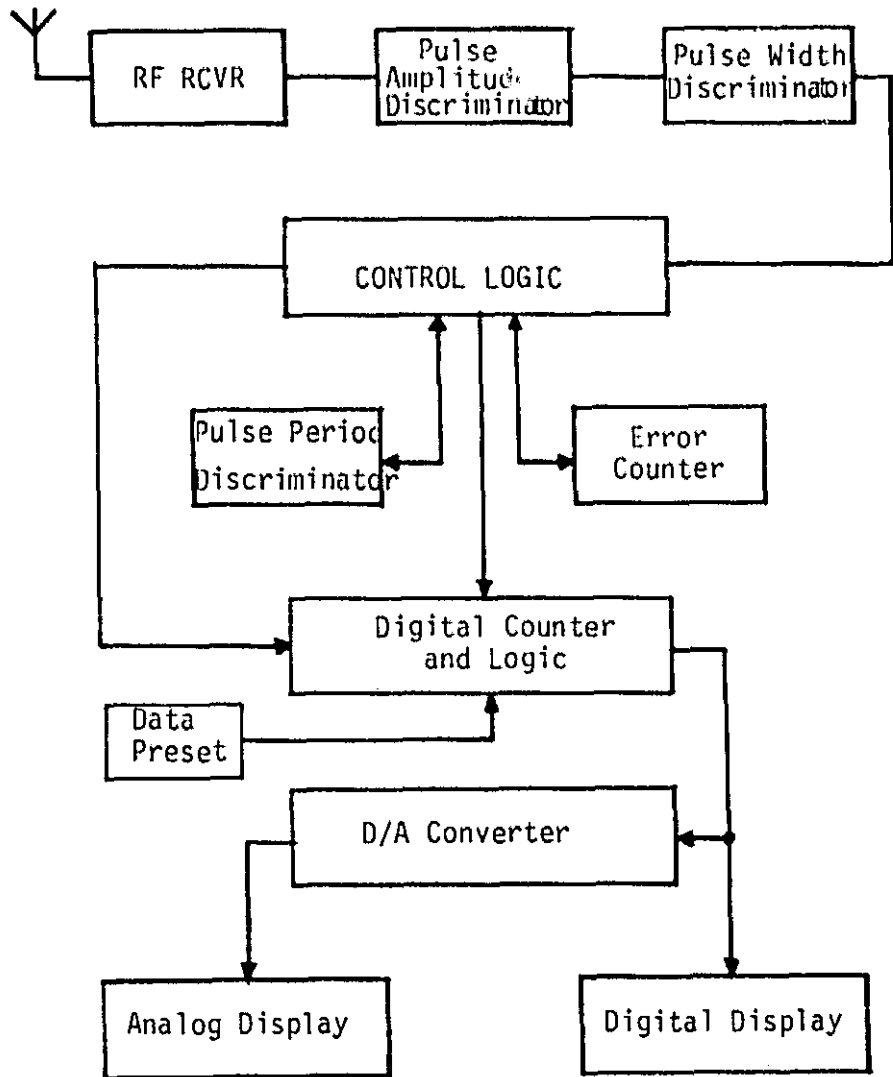


FIG. T 5 DIGITAL PROCESSING UNIT BLOCK DIAGRAM

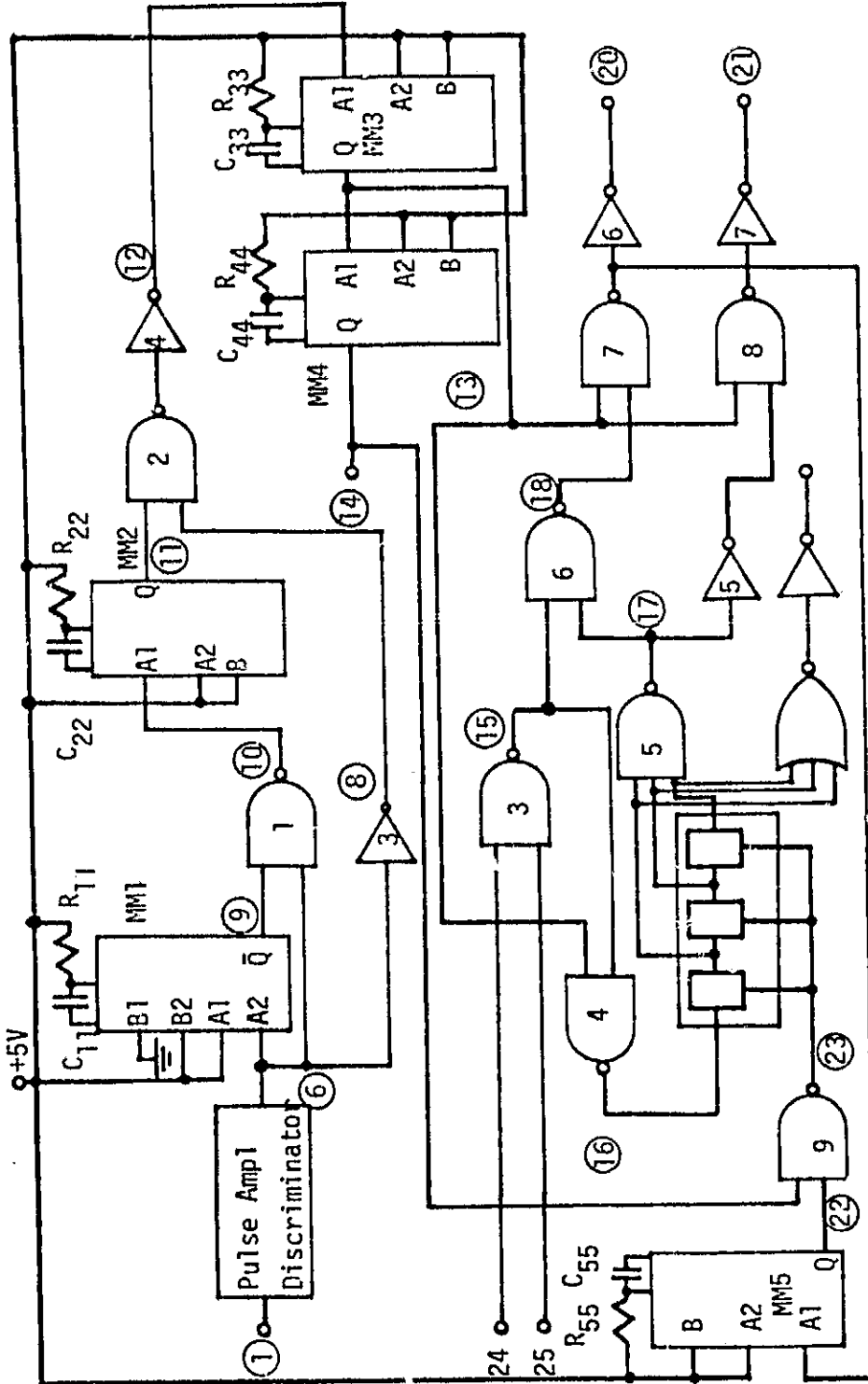


FIG. T 6 CONTROL LOGIC CIRCUIT DIAGRAM

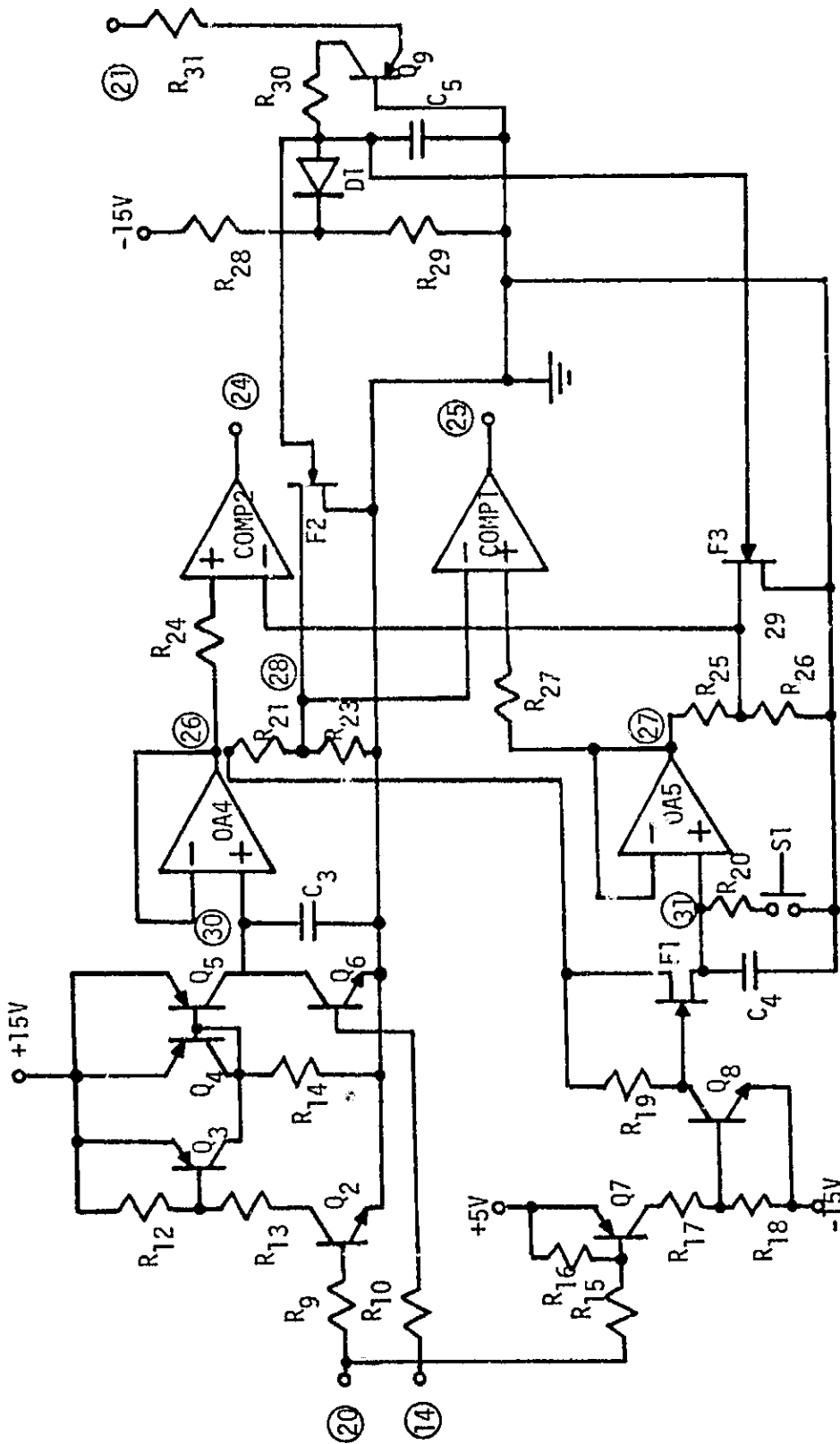


FIG. T 7 PULSE PERIOD DISCRIMINATOR CIRCUIT DIAGRAM

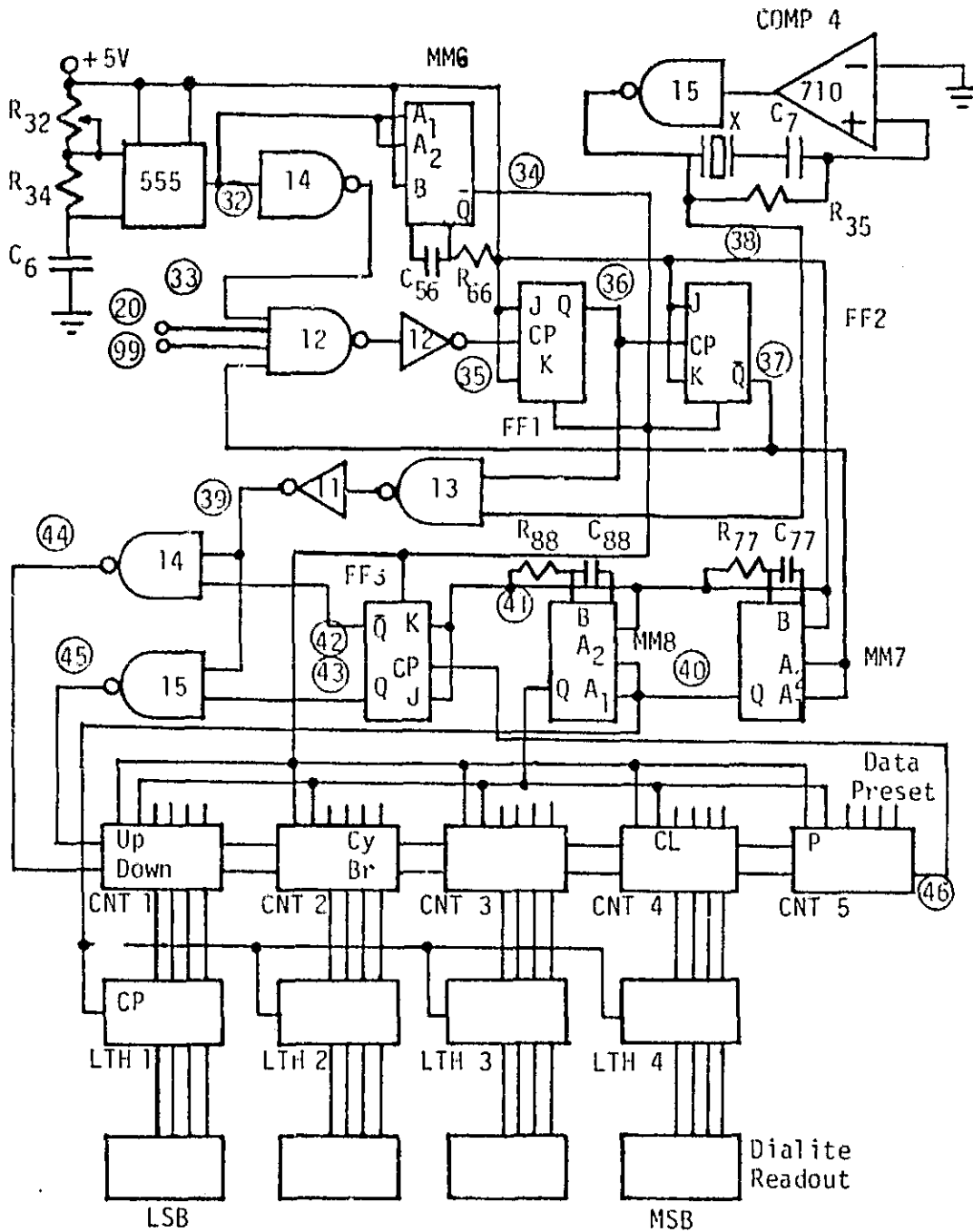


FIG. T 8 DIGITAL COUNTER AND LOGIC CIRCUIT DIAGRAM

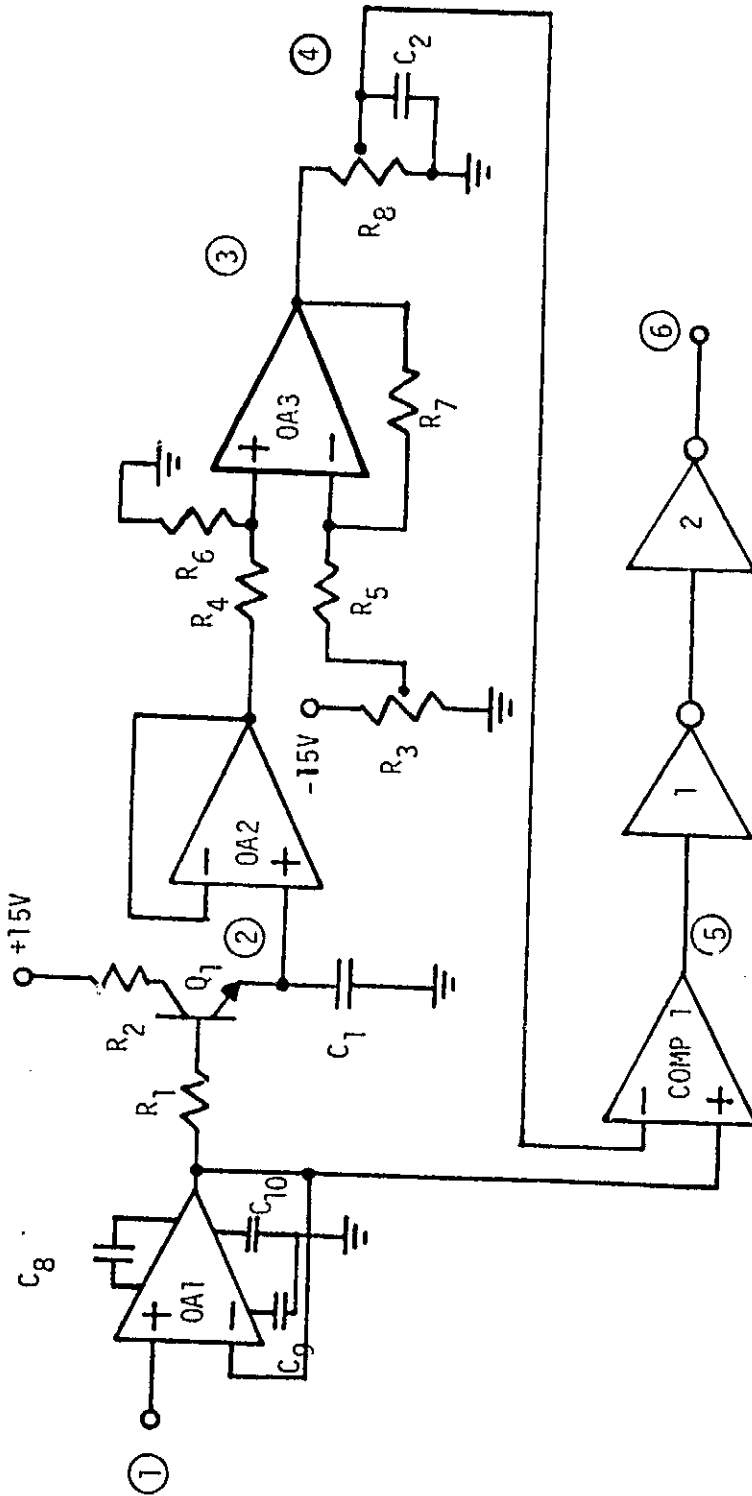


FIG. T 9 PULSE AMPLITUDE DISCRIMINATOR CIRCUIT DIAGRAM

DEVELOPMENT OF pO_2 AND pH SENSORS

III

In this period of time a miniature pH glass electrode which was realistically small, yet physically strong, was first constructed and then evaluated. A hydrogen ion sensitive glass, corning 015 glass (1.0 mm O.D.; 0.25 mm wall thickness) was used in constructing the pH glass electrode. The inner electrolyte was a solution of 0.1N HCl and the inner reference electrode was an Ag/AgCl electrode. The Ag/AgCl electrode was made from a silver wire (0.127 mm in diameter 99.9% purity) by the conventional electrolytic method. The hydrogen ion sensitive glass tubing was first sealed under direct flame. The average thickness of the sealed end was 0.484 mm compared to a wall thickness of 0.250 mm. The sealed glass tube was then filled with the inner electrolyte, 0.1N HCl solution. The inner reference electrode, the Ag/AgCl wire was placed inside the filled glass tube, and care was taken to avoid any formation of air bubbles. For the insulation of the glass electrode, a thin layer of the silicone fluid (Dow Corning 704) was placed on top of the inner electrolyte, and a silicone lubricant was put on top of the silicone fluid. These insulating materials were used to minimize the loss of the inner electrolyte due to evaporation. A coaxial shielded cable (Belden 83265) was soldered to the Ag/AgCl wire and was sealed with epoxy resin to a plexiglass supporter. Figure I shows the assembly of the pH glass electrode.

In this study, an amplification system was integrated into the pH glass electrode in order to widen the effective range of measurable pH values. An integral circuit FET input operational amplifier (AD503J, Analog Devices) was used. The input impedance of this amplifier was 10^{12} ohms, which was sufficiently high for this investigation. Different resistors were used in this amplification circuitary and average gain values of 4.41, 7.33, 11.38, and 16.43 were obtained.

The in vitro evaluations of the constructed pH glass electrode were carried out using both the reference pH buffer solutions and blood plasma as testing

medium. A constant temperature circulator (Haake Model KT41) was used to maintain a constant temperature. A digital voltmeter (Model 3440A, Hewlett Packard) and a strip chart recorder (Model 680, Hewlett Packard) were used for reading and recording the e.m.f. values of the electrode.

The linearity between the e.m.f. value of the electrode and the pH value of the test solution was determined. This calibration was done at 36°C in reference solutions, of pH 5.912-9.780. The electrode surface area was then altered by coating the surface area with insulated epoxy resin in order to investigate the effects of the electrode surface area on the electrode performance. The hysteresis phenomena due to the change in pH value and temperature were studied in the ranges of pH 5.912-9.780 at 36°C and of temperature 30-42°C respectively. Also, the stability of the electrode performance was evaluated by measuring the e.m.f. value in the following two ways: (a) continuous measurement of the e.m.f. value of the electrode in a reference solution of pH = 6.963 at 36°C, and (b) measurement of the e.m.f. values in three reference solutions of pH = 5.912, 6.963 and 7.877 at 36°C every fifth day throughout the operational lifetime of the electrode.

The temperature effects on the electrode were also studied at temperatures of 25, 30, 35 and 40°C in four reference solutions of pH = 6, 7, 8, and 9 at 25°C. The response time of the electrode was measured by recording the transient response of the e.m.f. at room temperature in a reference solution (pH = 7.00 at 25°C) and in blood plasma.

The in vitro evaluation in blood plasma was done aerobically at 36°, and all the experimental procedures were identical to those aforementioned.

Calibration of the constructed electrode is required to relate the potential and pH value of the tested solution. Thirteen pH glass electrodes with different lengths were used in this evaluation. Each electrode was calibrated with and without the FET amplification system. Each electrode was calibrated in 5 reference

buffer solutions with pH values of 5.912, 6.963, 7.877, 8.828 and 9.780 at 36°C. Our calibration tests showed that a good linear relationship existed between the electrode potential and the pH value of the buffer solutions. Figure II shows a typical calibration curve for a miniature pH glass electrode.

The results show that a good linear relation existed between the electrical potential of the glass electrode and the measured pH value. However, the response was relatively poor in the strongly alkaline solution, pH = 9.780 at 36°C in this study. This observation has been made by others with much larger pH glass electrodes.

The glass electrode potential is temperature-dependent. In this study, six miniature glass electrodes were used in the evaluation of the temperature dependence. Different pH buffer solutions (pH = 6, 7, 8 and 9 at 25°C) were used as the testing solutions, and the potential of the glass electrode was measured in these solutions at 25, 30, 35 and 40°C. Because the pH value of the reference solution was temperature dependent in itself, the evaluation of the experimental measurements took this correction into consideration. Figure III shows a typical temperature dependence of a miniature pH glass electrode. An average value of $-1.51 \text{ mv}/^\circ\text{K}$ at pH = 7 for six electrodes without the FET first stage amplification system was obtained. This value for temperature dependence is a function of pH values, with a trend to becoming larger in higher pH solutions. However, the variation was minute, and the output of the electrode could be temperature compensated electronically.

Glass electrodes usually show time-varying characteristics. In general, the hydration of the glass membrane and the asymmetry potential cause this variation. In this work, ten miniature pH electrodes were used in the evaluation of the time variation of the electrode potential. The electrode potential was continuously recorded for about 24 hours in a reference solution of pH = 6.963 at 36°C. The time variation of the measured pH value was compared to the initial pH value which was 6.963. The absolute potential change ranged from 3 mv to 25 mv over a period of 24

hours. Since the temperature and the pH value were kept constant throughout these measurements, neither pH nor temperature hysteresis effect was expected. The trend of this time variation for all the electrodes studies could not be predicted, i.e., the electrode potential might drift upward or downward. However, our experimental results show that the average absolute pH drifting over a seven hour period of time was 1% of the pH reading.

The pH and temperature hysteresis effects on the glass electrode were also investigated. Our results show that the change in pH values due to pH hysteresis effect was less than 0.5% of the assigned pH values of the reference solutions.

For the temperature hysteresis effect, the e.m.f. was measured in a reference solution (pH = 7.00 at 25°C) over a temperature range of 30-42°C. Over this temperature range, the pH value of the reference solution varied between 6.960 and 6.944. A pH hysteresis effect in this minute pH range could be considered negligible.

In vitro evaluation of the miniature pH glass electrode in blood plasma was also performed. In this study, the pH value of blood plasma was regulated by changing the concentration of bicarbonate ions. This in vitro evaluation was carried out aerobically at 36°C. The pH measurements of the blood plasma, pH and temperature hysteresis effects on the electrode performance, the time variation of the electrode potential, and the response time of the pH glass electrode in the blood plasma were investigated.

Each blood plasma sample had a total volume of 25 ml. An amount between 0 and 33 milli-equivalents of NaHCO_3 was added to the plasma. This gave a pH value calculated from the Henderson-Hasselbalch equation of the blood plasma at 36°C of 7.471 to 8.229. Figure IV shows a typical in vitro calibration of the developed miniature pH glass electrode. There is a deviation between the experimentally

measured pH value and the theoretically predicted pH value in the in vitro blood plasma measurements. An average percentage deviation of $1.2 \pm 1.1\%$ was found.

Glass membranes are usually considered thermogenic. Our in vitro evaluation used blood plasma, and the electrode did not appear to have any deterioration nor observable change on its performance over a 30 hour experimental time. This did not, however, present a sufficient evaluation of the electrode performance in blood. Further study and in vivo animal evaluation of the electrode is needed and will be performed.

In the research period of time, a miniature pCO_2 electrode for possible CO_2 measurement in a biological system was also constructed and evaluated. The pCO_2 electrode employed a miniature pH glass electrode was evaluated in both gas and liquid phases.

The pCO_2 electrode developed is a modified miniature pH glass electrode which was small yet large enough to remain physically strong. The details of the construction of this pH electrode have been described above. A micro-calomel electrode (9987-116 Veriflo Corp.) was employed in this unit as a reference electrode. Figure V shows the structure of the pCO_2 electrode. The housing unit for the electrode was made from plexiglass. The overall diameter of the tip including the housing was 2.5 mm. A Teflon membrane of the thickness of 1.0 mil (FD 100, Delextric Corp.) was used as the CO_2 permeable membrane. The reference solution in the pCO_2 electrode contained 0.01 M sodium bicarbonate and 0.1M potassium chloride. The small amount of potassium chloride solution was intended to stabilize the calomel reference electrode.

The characterization of the pCO_2 electrode was carried out in vitro in both gas and liquid media. The potential difference between the pCO_2 electrode and the calomel reference electrode was measured using an electrometer (Keithley 610C). The

output of the electrometer was then fed into a strip chart recorder (Model 680, Hewlett-Packard) and a digital voltmeter (Model 3440 A, Hewlett-Packard). All electrical units had a common ground.

The gas-phase evaluation of the $p\text{CO}_2$ electrode was carried out at room temperature, $\sim 20^\circ\text{C}$. Factory-premixed gas mixtures of different $\text{CO}_2 - \text{N}_2$ compositions were used. Five compositions of 2, 6, 10, 20 and 40% CO_2 balanced with nitrogen gas mixture were used. Other composition gas mixtures were obtained from these five gas mixtures. The gas composition was analyzed using a gas chromatograph (Model 5750, Hewlett-Packard).

The liquid-phase evaluation of the $p\text{CO}_2$ electrode was carried out in saline solution which was equilibrated with Different $\text{CO}_2 - \text{N}_2$ gas mixtures. The procedure and analysis were similar to those used in the gas-phase evaluation.

The pH response of the miniature pH glass electrode was important in providing a basis for later evaluation of its performance as a $p\text{CO}_2$ electrode. Thus, all the pH glass electrodes, used in the $p\text{CO}_2$ is electrode system, were first evaluated to determine their pH response. If the overall performance of a tested pH electrode was satisfactory, the pH electrode was then used for $p\text{CO}_2$ measurement. In vitro calibration of the $p\text{CO}_2$ electrode was first undertaken. Eight electrodes were used in this phase of the study. All the $p\text{CO}_2$ electrodes were tested at room temperature, about 20°C , in both gas and liquid phases. The concentration of carbon dioxide varied between 2 and 42 mole %.

In principle, the measured electrode potential is linearly proportional to the logarithm of the CO_2 concentration. Figure VI shows a typical calibration curve of a $p\text{CO}_2$ electrode. A good linear relation exists between the electrode potential and the logarithm of CO_2 concentration. The results also indicate the electrode performance is not affected by the testing medium whether it is in the gas or liquid phase.

For each $p\text{CO}_2$ electrode constructed, the slope of this linear relation varied, and individual calibration for each electrode was required.

The temperature effect on the performance of the $p\text{CO}_2$ electrode was investigated between 20 and 60°C at constant CO_2 concentration in the liquid phase. The testing $p\text{CO}_2$ electrode was submerged in a saline solution placed in a constant temperature bath and a constant stream of CO_2 bubbled through the saline solution. Constant stirring of the saline solution was maintained throughout.

The solubility of the carbon dioxide in the saline solution is a function of temperature. Thus, even when a fixed composition CO_2 gas was used in equilibrating with the saline solution, correction of the CO_2 composition due to the solubility of CO_2 at different temperatures must be considered. In this study, a 9.6 mole % CO_2 gas mixture (factory premixed 10% gas mixture) was used for equilibrating with the saline solution, and its solubility in the saline solution over the temperature range was then taken into consideration. The Bensen absorption coefficients of CO_2 in 1.195 and 3.659 molar NaCl solution over the temperature range of 0-60°C was used to extrapolate the Bensen absorption coefficient of CO_2 in saline solution (1.541 molar NaCl solution) over the temperature range of 0-60°C. The solubility of the CO_2 in a solution can be expressed as:

$$C = aP$$

where C is the concentration of CO_2 in solution, a is the Bensen absorption coefficient at that temperature and P is the partial pressure of CO_2 in the vapor phase. Because the measured electrode potential of the $p\text{CO}_2$ electrode is linearly proportional to the logarithm of CO_2 concentration in the solution, thus an effect of the correction on the measured electrode potential corresponds to the solubility of the CO_2 at different temperatures can be obtained. This potential value was used in the correction of the measured electrode potential. In our

study, the potential reading at 20°C was chosen arbitrarily as the reference and set to zero. Figure VI shows a typical temperature effect on the electrode potential and the temperatures.

Both temperature and $p\text{CO}_2$ hysteresis effects on the $p\text{CO}_2$ electrode were also investigated. Our results show that both effects on the performance of the $p\text{CO}_2$ electrodes are negligible.

Three $p\text{CO}_2$ electrodes were used in the tests of long term stability in the gas and liquid phase over a period of more than 20 hours at a constant composition of 2.1 mole % CO_2 . The absolute electrode potential drifted approximately 1.5-2.0 mv per 10 hours in gas and liquid phase testings. This drifting in potential represented approximately 9-10% change in CO_2 over 10 hours which was reasonable.

The stability of the $p\text{CO}_2$ electrode for long term continuous measurement was affected by the degeneration of the bonding between the non-active coating and the glass electrode, the deterioration of the gas permeable membrane and the inherent asymmetric characteristics of the glass electrode. These characteristics, unfortunately, hindered the long-term stability of the $p\text{CO}_2$ electrode constructed.

The response time of the $p\text{CO}_2$ electrode was also evaluated. A step change in CO_2 construction was first provided and the response time required for the $p\text{CO}_2$ electrode was then recorded. For a gas flow rate of 6.5 ml/sec. it required 4 minutes to reach 90% of the equilibrium value. This is considered relatively slow and further improvement in the gas membrane will be desirable.

In future work, in vitro evaluation of the electrode in blood plasma is desirable and will be undertaken.

During this research period of time, and paper intituled "Development of a Miniature pH Glass Electrode with Field Effect Transistor Amplifier for Biomedical Applications," was accepted by Medical and Biological Engineering for publication.

Another paper entitled "Development of A miniature pCO₂ Electrode for Miomedical Applications" was submitted for publication. In both articles, the support by this research grant NGR-36-027-053 from the NASA - Ames Research Center is gratefully acknowledged.

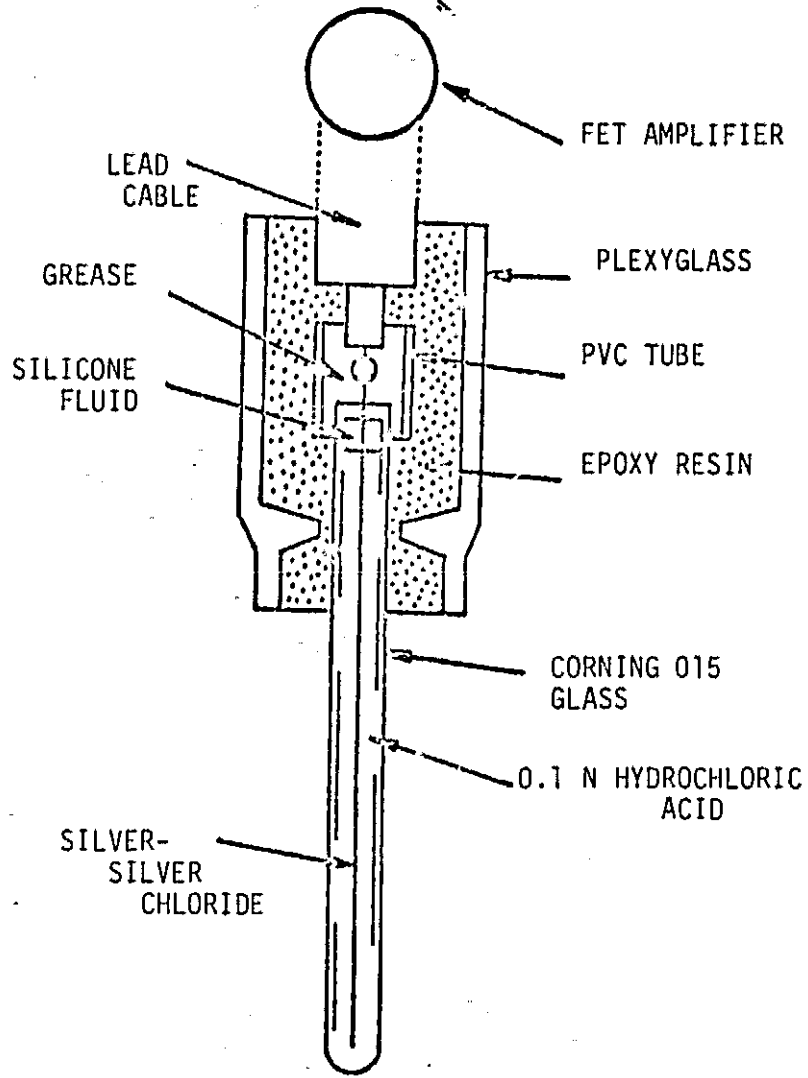


Figure I Assembly of a Miniature pH Glass Electrode

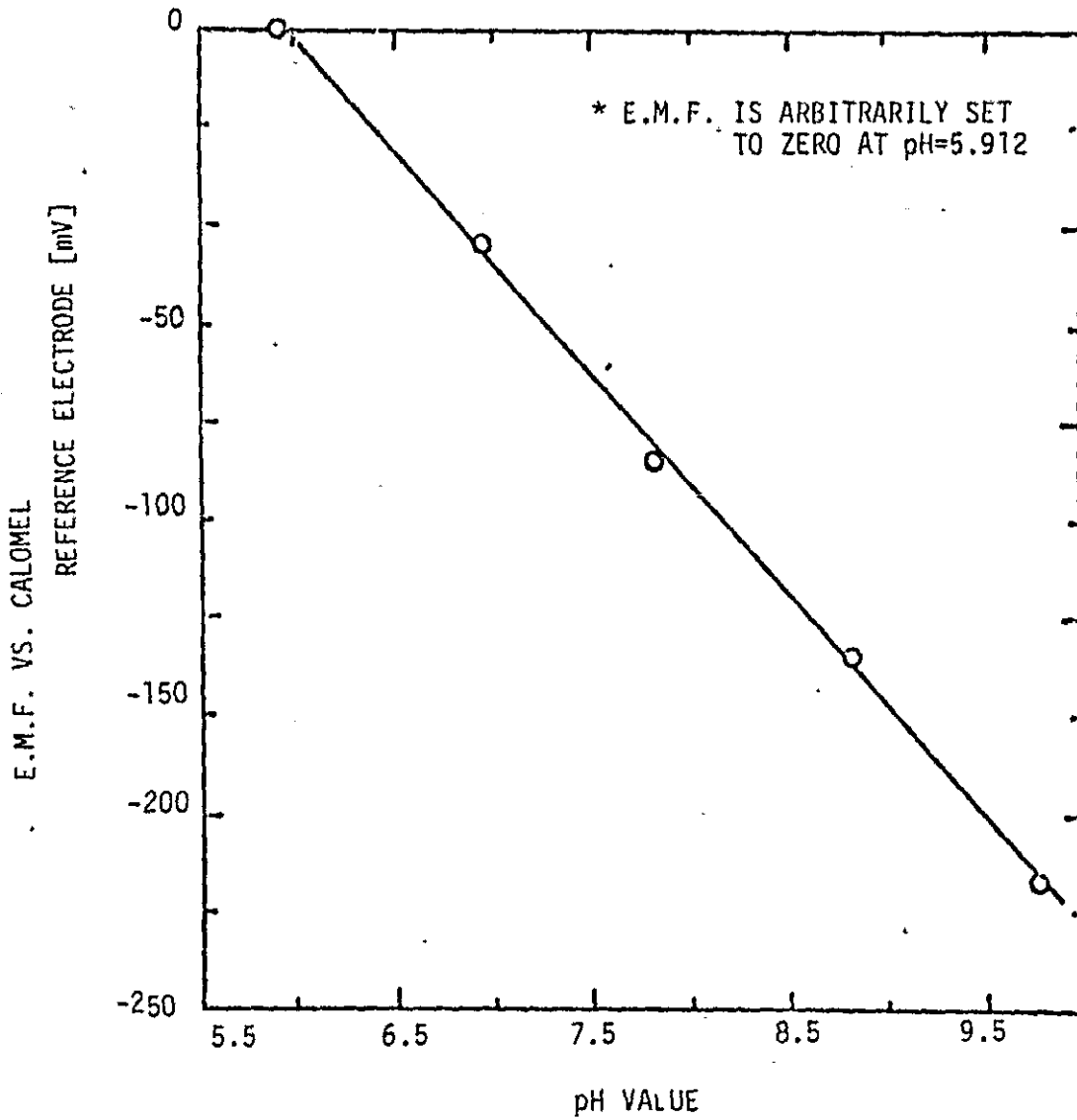


Figure II A typical Calibration Curve of the Miniature pH Glass Electrode at 36°C

* E.M.F. IS ARBITRARILY SET TO ZERO
AT pH=7 AND 298 DEGREE K.

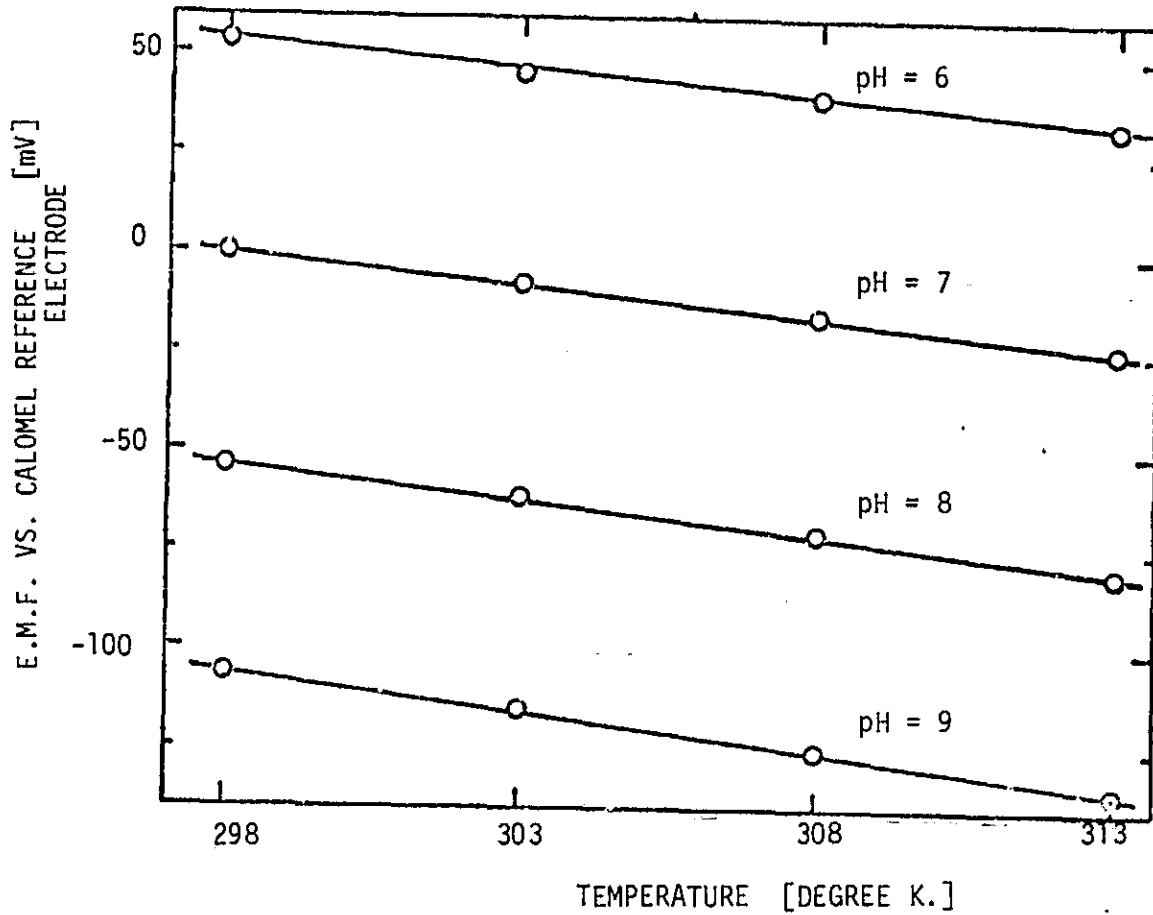


Figure III Relation between the e.m.f. and Temperature at Different pH Values

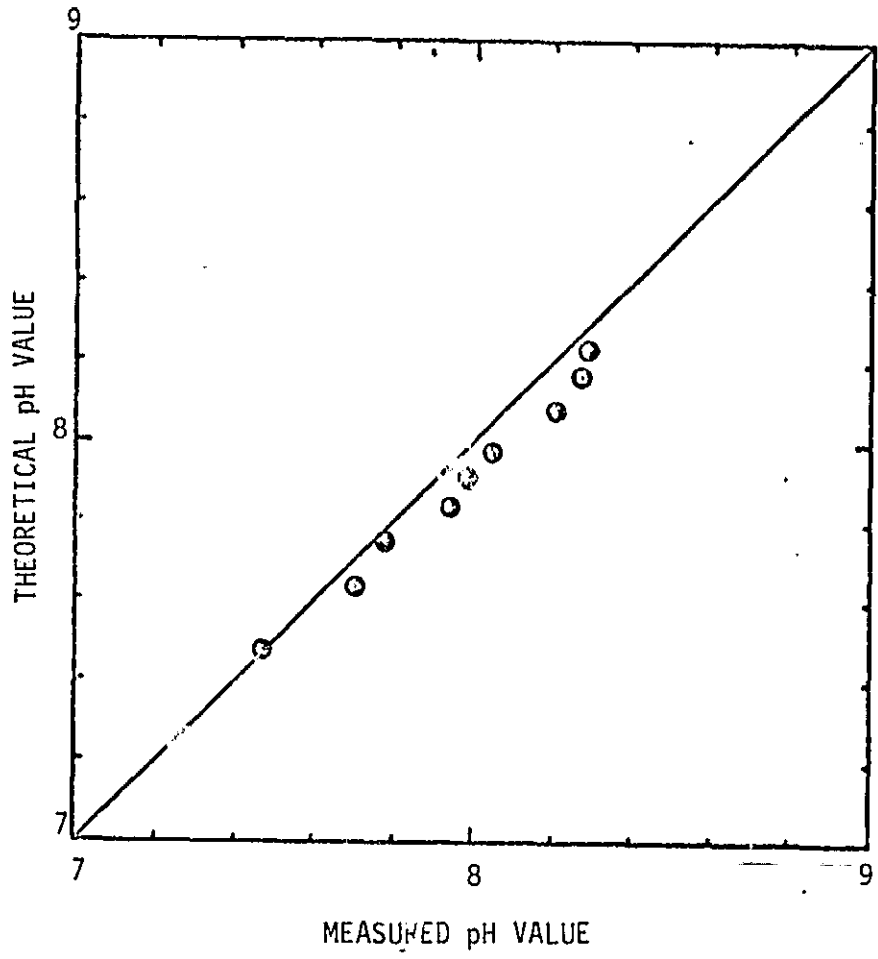


Figure IV Relation between the Theoretical and the Measured pH Values, in Blood Plasma, at 36°C

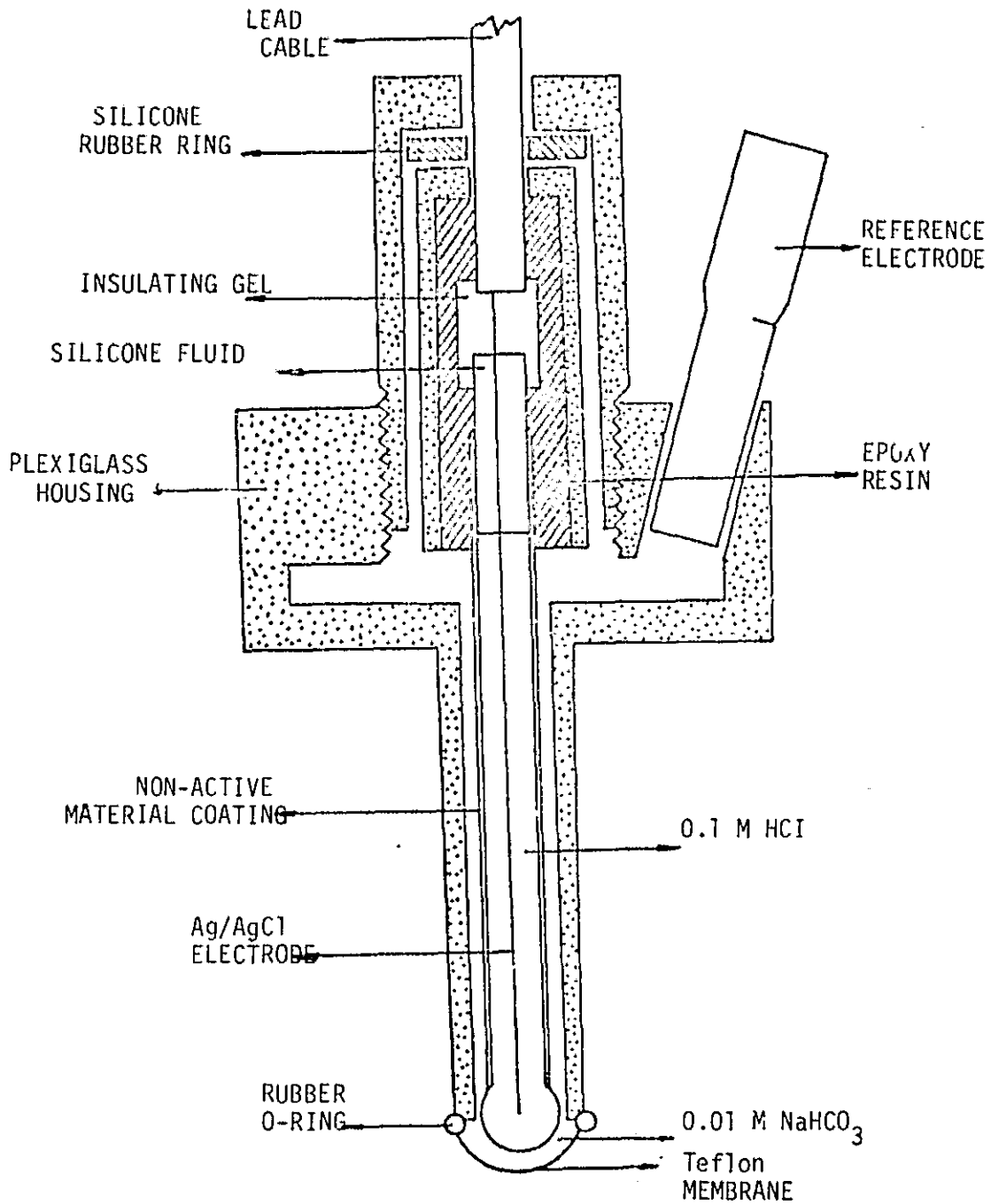


Figure V Assembly of a Miniature $p\text{CO}_2$ Electrode

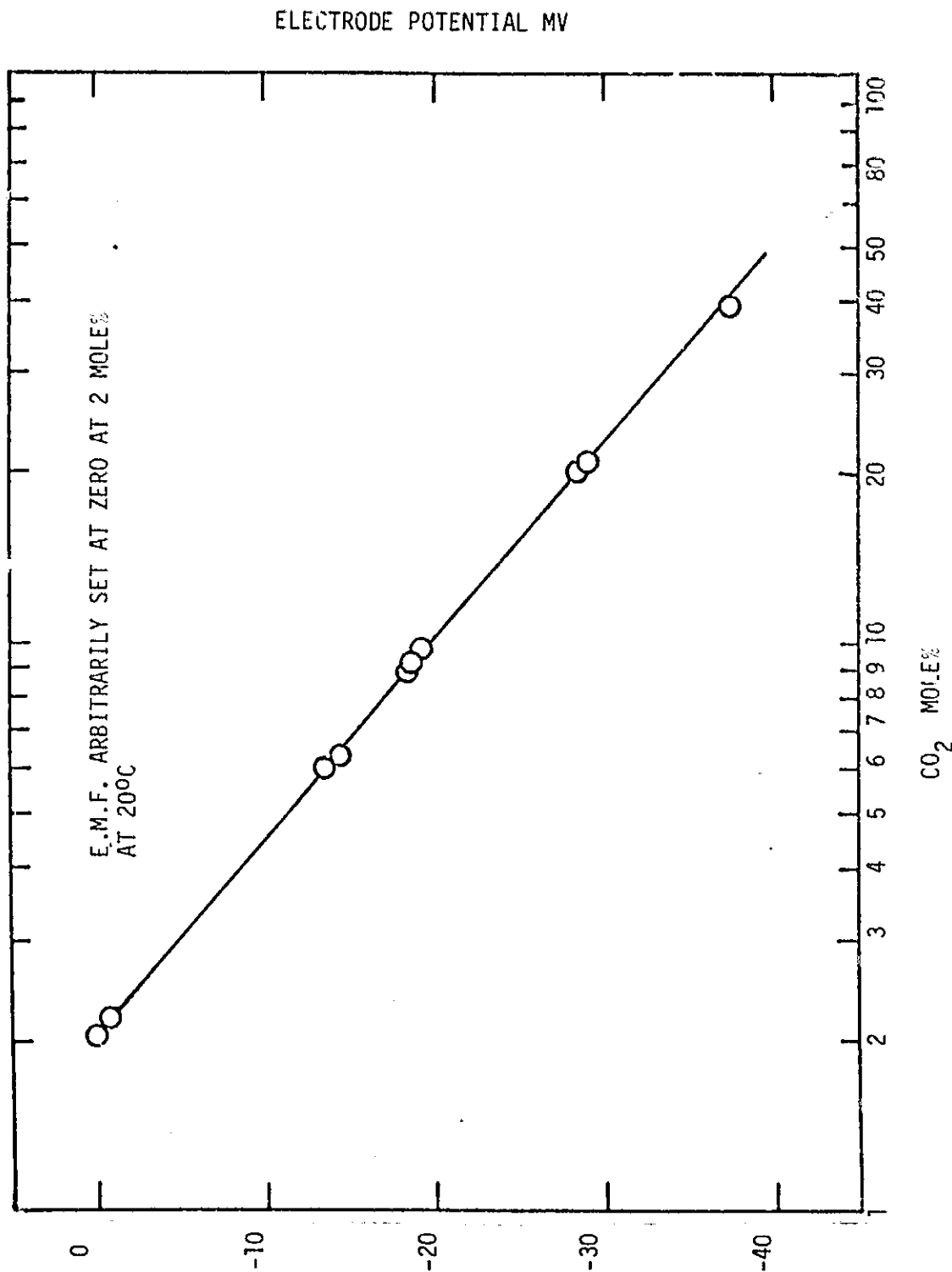


Figure VI A Typical calibration curve of the Miniature pCO₂ Electrode at 20°C

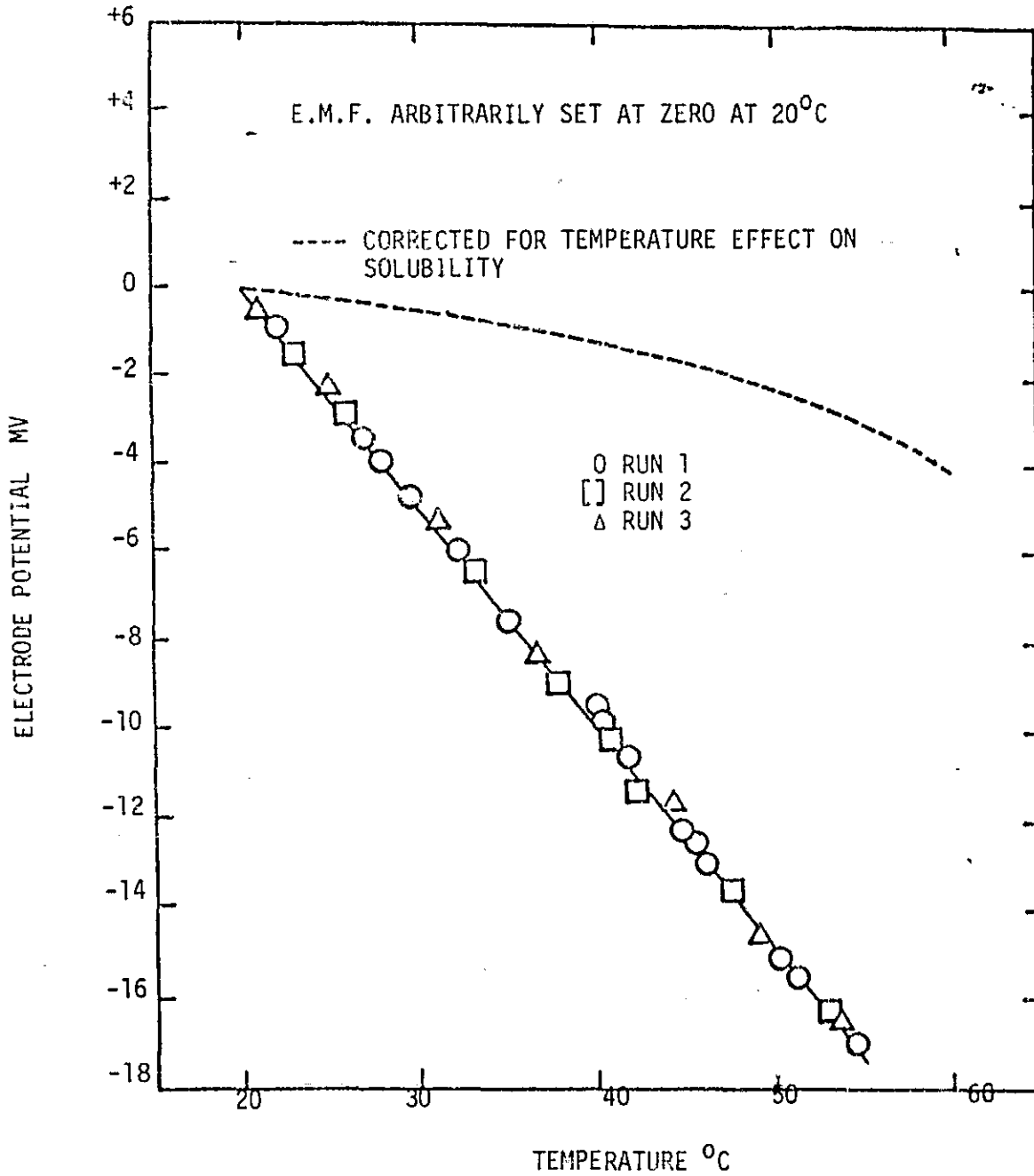


Figure VII Temperature Effect on the $p\text{CO}_2$ Electrode Potential at 9.6 mole % CO_2 in Saline Solution